
Doctoral Dissertations

Student Theses and Dissertations

Fall 2022

LATERALLY HETEROGENEOUS SEISMIC ANISOTROPY INVESTIGATED BY SHEAR WAVE SPLITTING ANALYSES

Yan Jia

Missouri University of Science and Technology

Follow this and additional works at: https://scholarsmine.mst.edu/doctoral_dissertations



Part of the [Geology Commons](#), and the [Geophysics and Seismology Commons](#)

Department: Geosciences and Geological and Petroleum Engineering

Recommended Citation

Jia, Yan, "LATERALLY HETEROGENEOUS SEISMIC ANISOTROPY INVESTIGATED BY SHEAR WAVE SPLITTING ANALYSES" (2022). *Doctoral Dissertations*. 3236.

https://scholarsmine.mst.edu/doctoral_dissertations/3236

This thesis is brought to you by Scholars' Mine, a service of the Missouri S&T Library and Learning Resources. This work is protected by U. S. Copyright Law. Unauthorized use including reproduction for redistribution requires the permission of the copyright holder. For more information, please contact scholarsmine@mst.edu.

LATERALLY HETEROGENEOUS SEISMIC ANISOTROPY INVESTIGATED BY
SHEAR WAVE SPLITTING ANALYSES

by

YAN JIA

A DISSERTATION

Presented to the Graduate Faculty of the
MISSOURI UNIVERSITY OF SCIENCE AND TECHNOLOGY

In Partial Fulfillment of the Requirements for the Degree

DOCTOR OF PHILOSOPHY

in

GEOLOGY AND GEOPHYSICS

2022

Approved by:

Kelly H. Liu, Advisor
Stephen S. Gao, Co-advisor
Katherine R. Grote
Abdulmohsin H. Imqam
Ying Shi

© 2022

Yan Jia

All Rights Reserved

PUBLICATION DISSERTATION OPTION

This dissertation consists of the following two articles, formatted in the style used by the Missouri University of Science and Technology:

Paper I, found on pages 5–37, has been published in *Geophysical Journal International*.

Paper II, found on pages 38–73, has been submitted to *Journal of Geophysical Research: Solid Earth*.

ABSTRACT

Numerous geophysical studies suggest that seismic anisotropy is a nearly ubiquitous property of the Earth's crust and upper mantle. In this study, we utilize the shear wave splitting technique to investigate the piercing-point-dependent azimuthal anisotropy beneath the northeastern edge of the Sichuan Basin in central China, and the spatial and temporal variations of anisotropy near the 2019 M7.1 Ridgecrest earthquake in California, respectively. A clear back azimuthal dependence of the splitting parameters and the lack of a 90° or 180° periodicity of azimuthal variation in the observed fast orientations provide strong evidence for the existence of piercing-point-dependent anisotropy beneath the Sichuan Basin. It is inferred that the observed anisotropy mainly comes from the upper asthenosphere at ~ 250 km and can be explained by a simple geodynamic model invoking absolute plate motion related to simple shear in the lithosphere-asthenosphere transitional layer and mantle flow deflected by the thick lithospheric root of the basin in the upper asthenosphere. In the vicinity of the 2019 Ridgecrest M7.1 earthquake sequence, significant spatial variations in the orientation and formation mechanisms of azimuthal anisotropy are observed. Specific findings include along-strike variations in fault zone width, an asymmetry in rock strength across the main fault in the area, confirmation of a proposed blind fault, and a temporal change in the orientation and strength of anisotropy that may reflect healing of fractures that were activated by the earthquake sequence.

ACKNOWLEDGMENTS

I would like to express my deepest appreciation to my advisors, Dr. Kelly H. Liu and Dr. Stephen S. Gao, for providing their consistent support and professional guidance. During the past five years, they have been not only dedicated to improving my academic research skills but also encouraging me to enhance my willpower. Without their enthusiastic and selflessly offered suggestions, I could not complete this dissertation or even accomplish my Ph.D. degree.

Besides, I am sincerely indebted to my committee members, Dr. Katherine R. Grote, Dr. Abdulmohsin H. Imqam, and Dr. Ying Shi, whose interdisciplinary insight and knowledge benefited me through my dissertation. I am also thankful to Dr. Jeffrey Cawfield, Ms. Patty Robertson, Ms. Megan Bilkey, and Ms. Sharon Lauck, who are the current and former faculties and staffs of Geosciences and Geological and Petroleum Engineering department, and Ms. Jade Sinnott, who is my graduate advisor, for all their patient assistances during my undergraduate and graduate careers.

I really appreciate all my friends and colleagues who helped and encouraged me a lot over the past five years. I would also like to acknowledge the former members of our geophysics group, especially Drs. Fansheng Kong and Muchen Sun, who steered me with their expertise during my study.

Finally, I would like to pay my special regards to my mother and father for their unconditional support. Their endless love, understanding, and encouragement enabled me to become better.

TABLE OF CONTENTS

	Page
PUBLICATION DISSERTATION OPTION	iii
ABSTRACT	iv
ACKNOWLEDGMENTS	v
LIST OF ILLUSTRATIONS	ix
LIST OF TABLES	xii
NOMENCLATURE	xiii
 SECTION	
1. INTRODUCTION	1
 PAPER	
I. A SYSTEMATIC INVESTIGATION OF PIERCING-POINT-DEPENDENT SEISMIC AZIMUTHAL ANISOTROPY	5
ABSTRACT	5
1. INTRODUCTION	6
2. DATA AND METHODS	10
3. RESULTS AND COMPARISON WITH MEASUREMENTS FROM PREVIOUS STUDIES	13
3.1. STATION ENH	15
3.2. STATION HFE	17
3.3. STATION LCH	18
4. DISCUSSION	20
4.1. EVIDENCE FOR PIERCING-POINT-DEPENDENT ANISOTROPY	20

4.2. ANISOTROPY DEPTH ESTIMATION	21
4.3. SYNTHETIC TEST	24
4.4. GEODYNAMIC IMPLICATIONS	26
5. CONCLUSIONS	30
ACKNOWLEDGMENTS	30
DATA AVAILABILITY	31
APPENDIX	31
REFERENCES	31
II. SEISMOGENIC LAYER AZIMUTHAL ANISOTROPY IN THE VICINITY OF THE 2019 M7.1 RIDGECREST EARTHQUAKE REVEALED BY SHEAR WAVE SPLITTING ANALYSIS	38
ABSTRACT	38
1. INTRODUCTION	39
1.1. SHEAR WAVE SPLITTING ANALYSIS AND SEISMOGENIC LAYER AZIMUTHAL ANISOTROPY	40
1.2. RATIONALE OF THE STUDY	41
2. DATA AND METHODS	43
3. RESULTS	44
3.1. STATION CA01	46
3.2. STATION CA03	47
3.3. STATION CA06	49
4. DISCUSSION	51
4.1. CYCLE SKIPPING	52
4.2. REGIONAL STRESS INDUCED ANISOTROPY (AREAS A, C, AND F) ..	54

4.3. ANISOTROPY ASSOCIATED WITH SURFACE AND BLIND FAULTS (AREAS B, D, AND E).....	55
4.4. ASYMMETRY IN ROCK STRENGTH ACROSS THE ELLF.....	57
4.5. POSSIBLE TEMPORAL VARIATIONS OF THE OBSERVED ANISOTROPY.....	57
5. CONCLUSIONS	59
ACKNOWLEDGMENTS.....	60
DATA AVAILABILITY STATEMENT.....	60
APPENDIX	61
REFERENCES.....	66
SECTION	
2. CONCLUSIONS	74
BIBLIOGRAPHY.....	76
VITA.....	80

LIST OF ILLUSTRATIONS

PAPER I	Page
<p>Figure 1. (a) Topographic map of the northeastern part of the Sichuan Basin showing major tectonic boundaries (thick purple dashed lines) and stations used in this study (red triangles with station name). The mapped area is marked by the red rectangle in the inset map of East Asia. The thin purple dashed line presents the boundary of the Sichuan Basin. The thick green and thin blue bars indicate the station-averaged and individual shear-wave splitting (SWS) measurements from different previous studies obtained from http://www.gm.univ-montp2.fr/splitting/DB/. (b) Previous SWS measurements at stations used in this study. Different colors represent different studies.</p>	9
<p>Figure 2. Events location.</p>	12
<p>Figure 3. Examples of SWS measurements (quality A) recorded by stations ENH, HFE, and LCH.</p>	13
<p>Figure 4. Summary of measurements at Station ENH.</p>	14
<p>Figure 5. Same as Figure 4 but for Station HFE.</p>	17
<p>Figure 6. Same as Figure 4 but for Station LCH.</p>	19
<p>Figure 7. PKS, SKKS, and SKS splitting parameters (quality A and B) from this study plotted at piercing point locations at different depths.</p>	21
<p>Figure 8. (a–g) Distribution of the standard deviation (SD) of spatially averaged fast orientations in 0.2° radius circles at the depth of 0, 100, 150, 200, 250, 300, and 350 km. The averaged SD results are indicated in the upper left corner of each map. The results plotted were resampled into a resolution of 0.1°. The red, blue, and pink bars indicate individual measurements of stations LCH, ENH, and HFE, respectively. (h) Anisotropy depth analysis for the SWS measurements based on the spatial coherence technique (K.H. Liu & Gao, 2011), resulting in an optimal depth of anisotropy at 250 km. The red triangle on the curve marks the depth with the minimum variation factor.</p>	23

Figure 9. Comparison of SWS measurements using synthetic seismograms generated using SPECFEB3D_GLOBE (a) and those from corresponding observed seismograms (b).....	25
Figure 10. Same as Figure 3 but for the SWS measurements computed from the synthetic seismograms for two station-event pairs.	27
Figure 11. A schematic model showing the mantle flow field beneath the study area.	29

PAPER II

Figure 1. (a) Distribution of seismic stations used in the study (black triangles) and earthquakes that occurred in 2019 (red dots). The green stars show the epicenters of the M6.4 (4 July 2019), and M7.1 (6 July 2019) earthquakes. The study area is marked by a blue rectangle. The inset map in the upper-right corner shows the location of the main map. WL: Walker Lane; ECSZ: Eastern California Shear Zone. (b) Fault network in the 2019 Ridgecrest aftershock zone. The grey, black solid, and black dashed lines indicate the Quaternary faults (Wills, 1988), and the surface ruptures (DuRoss et al., 2020; Ponti et al., 2020) and the blind faults (Hauksson et al., 2020; Plesch et al., 2020) formed after the M7.1 Ridgecrest earthquake sequence, respectively. The colored polygons and histograms show the distribution and variations of the orientation of the maximum horizontal compressive stress (SHmax) in different subzones (I-V) of the mapped area (Sheng & Meng, 2020). In each of the histograms, the columns from left to right represent the SHmax in the time-period prior to the M6.4 foreshock, between the M6.4 and M7.1 earthquakes, and after the M7.1 mainshock, respectively. (c) A plot of earthquake magnitudes against origin times. (d) Distribution of earthquakes projected to Profile A-B in (a). (e) Distribution of earthquakes projected to Profile C-D in (a).....	42
Figure 2. Examples of SWS measurements from Stations CA01, CA03, and CA06.....	45
Figure 3. (a) Resulting SWS parameters of Station CA01 plotted at the epicenters. The orientation of the bars represents the fast orientation, and the length is proportional to the splitting time. The color of the bars indicates focal depths, and the rose diagram is created using all the fast orientation measurements from this station. (b) Absolute angular difference between fast orientations and SHmax direction (Sheng & Meng, 2020). (c) Splitting time measurements. (d) Ray path normalized splitting times. S-M ELLF: South-Main branch of the ELLF; S-W ELLF: South-West branch of the ELLF; C-S-N BF: Cross-South-North blind fault; C-S-S BF: Cross-South-South blind fault. S-C-S-R: Short-Cross-Sinistral-Rupture.....	46

Figure 4. Same as Figure 3 but for Station CA03. North SLLF: north branch of the SLLF.	48
Figure 5. Same as Figure 3 but for Station CA06.....	50
Figure 6. (a) Same as Figure 3a but for SWS parameters observed by all three stations. The shaded areas are subdivisions of the whole study area. Measurements in the black circle near the center of the diagram show temporal variations. (b) Same as Figure 3b but for all the measurements from the three stations.....	51
Figure 7. (a) Resulting splitting times plotted at the epicenters. (b) Normalized splitting time. Different areas are marked by the yellow polygons.	54
Figure 8. Measurements from 7 events in the black circle in Figure 6a that show apparent temporal variations.....	58

LIST OF TABLES

PAPER I	Page
Table 1. <i>SWS</i> measurements from previous and the present studies.	15

NOMENCLATURE

Symbol	Description
ϕ	Fast Polarization Orientation
δt	Splitting Time

SECTION

1. INTRODUCTION

Seismic anisotropy, which is a term used to describe the azimuthal dependence of seismic velocity on the propagation direction, is a nearly pervasive characteristic of the Earth's crust and upper mantle (e.g., Crampin, 1987; Gao et al., 1994; Hess, 1964; Y. Liu et al., 2008; Mainprice & Nicolas, 1989; Miller & Savage, 2001; Peng & Ben-Zion, 2004; Silver & Chan, 1991). An anisotropic medium typically contains an internal structure with directionally aligned crystals or cracks (Crampin, 1987). As one of the most effective tools in the studies of the Earth's interior structures, in this study, we employ the shear wave splitting (SWS) technique to measure the seismic azimuthal anisotropy in the upper crust and upper mantle (Ando et al., 1983; Crampin, 1991, 1994; Fuchs, 1977; Y. Liu et al., 2008; Long & Silver, 2009; Silver & Chan, 1991; Silver, 1996; Savage, 1999; Peng & Ben-Zion, 2004; Vinnik et al., 1992). When a shear wave propagates through an anisotropic medium, it splits into two nearly perpendicular shear waves with different velocities (Silver, 1996; Savage, 1999; Long & Silver, 2009). The orientation and the strength of anisotropy are quantified by two splitting parameters, including fast orientation (ϕ), which is the vibration orientation of the fast wave, and splitting time (δt), which is the time separation between the fast and slow waves.

In the upper mantle, seismic anisotropy is mainly caused by the strain-induced lattice preferred orientation (LPO) of anisotropic minerals, especially olivine (Zhang & Karato, 1995). The formation of LPO in the upper mantle can be simply divided into two

processes. The anisotropy in the lithosphere is generally related to vertically coherent deformation, which is caused by horizontal compression. The fast orientation here is perpendicular to the maximum horizontal shortening direction (Silver & Chan, 1991; Silver, 1996; Fouch & Rondenay, 2006). On the other hand, in the upper asthenosphere, the anisotropy is usually attributed to the simple shear strain induced by the relative movement between the lithosphere and asthenosphere and leads to an APM-parallel fast orientation (Ben Ismail & Mainprice, 1998; Long & Silver, 2009; Ohuchi & Irifune, 2013).

Generally, stress-induced anisotropy and structure-induced anisotropy are the two major forms of upper crustal anisotropy. Stress-induced anisotropy is generally attributed to the structures of fluid-filled microcracks (Boness & Zoback, 2004; Crampin, 1978, 1987, 1993; Leary et al., 1990). The fast orientation is mostly parallel to the maximum horizontal compressive stress (SHmax) direction and is related to the local stress field. Structure-induced anisotropy is usually observed in the active fault zone and other complicated structural areas, and mainly controlled by tectonic processes and shows fault strike parallel fast orientation (Boness & Zoback, 2006; Z. Li & Peng, 2017; Zinke & Zoback, 2000; Zhang & Schwart, 1994). In some specific regions, a mixture of azimuthal anisotropy-forming mechanisms can be observed (Cochran et al., 2003; Peng & Ben-Zion, 2004).

Most of the previous studies of seismic anisotropy were based on the assumption of spatial invariant anisotropic structures (e.g., Y. Liu et al., 2008; Silver & Savage, 1994) and usually led to misinterpretation in complex tectonic regions. To efficiently explore the local-scale laterally heterogeneous seismic anisotropy in different layers of

the Earth, as well as the associated formation mechanisms, we divided the examination into two aspects, including the study of piercing-point-dependent anisotropy in the upper mantle observed beneath the northeast edge of the Sichuan Basin in central China, as well as the spatial and temporal variation of seismic anisotropy in the shallow crust in the vicinity of the 2019 M7.1 Ridgecrest earthquake, California.

In the first project, we provide a systematic investigation of piercing-point-dependent anisotropy, which is one of the typical laterally heterogeneous anisotropy and has previously been neglected, by using the teleseismic data from 3 seismic stations located on the northeast edge of the Sichuan Basin in central China. This kind of seismic anisotropy can usually be observed near the boundary between two or more tectonic regions, and the observed splitting parameters at the station vary as functions of ray piercing locations and also display inconsistent fast orientations (K.H. Liu & Gao, 2013). To qualify the piercing-point-dependent anisotropy in the upper mantle, we use the P-to-S convert waves at the core-mantle boundary on the receiver side (Ando et al., 1980; Silver & Chan, 1991), including SKS, SKKS, and PKS, hereafter called XKS phases collectively. In addition, we estimate the depth of the anisotropy source based on the SWS observations using the spatial coherency method (K.H. Liu & Gao, 2011; Gao & K.H. Liu, 2012) and examine the reliability of the results based on the overlap of the first Fresnel zones and synthetic seismogram generation. We next explore the associated geodynamic implications and establish a model showing the mantle flow field beneath the Sichuan Basin.

On July 6th, 2019, an M7.1 earthquake occurred near Ridgecrest, California. Together with the M6.4 foreshock and tens of thousands of aftershocks, these

earthquakes made up the 2019 Ridgecrest earthquake sequence and activated a complex fault network (e.g., Barnhart et al., 2019, DuRoss et al., 2020; C. Liu et al., 2019; Ponti et al., 2020; Ross et al., 2019, Shelly, 2020). These fractures in the top several kilometers of the Earth associated with fault zones and fluid-filled micro-fractures formed in response to regional compressive stress may result in directional dependence of the traveling speed of seismic waves. Such a dependence reflects the seismic azimuthal anisotropy in the upper crust and can decipher the lateral and vertical distributions as well as the orientation of the fractures. Therefore, in the second project, we measure the local S data obtained from three portable stations, which provide the data recording for up to half a year after the M7.1 mainshock, to characterize the possible coseismic or postseismic variation of upper crustal anisotropy. Then we identify the mechanisms of anisotropy formation in different areas. We also investigate the spatial and possible temporal variations of anisotropy, to verify previous assumptions about stress field status, fault structures, and asymmetric rock strength in the study area. Besides, a possible healing process for activated fractures has been proposed based on the observations of temporal variation in anisotropy.

PAPER

I. A SYSTEMATIC INVESTIGATION OF PIERCING-POINT-DEPENDENT SEISMIC AZIMUTHAL ANISOTROPY

ABSTRACT

The vast majority of teleseismic XKS (including SKS, SKKS and PKS) shear wave splitting studies interpret the observed splitting parameters (fast orientation and splitting time) based on the assumption of a spatially invariant anisotropy structure in the vicinity of a recording station. For such anisotropy structures the observed splitting parameters are either independent of the arriving azimuth of the seismic ray paths if the medium traversed by the ray paths can be represented by a single layer of anisotropy with a horizontal axis of symmetry (i.e., simple anisotropy), or demonstrate a periodic variation with respect to the arriving azimuth for a more complicated structure of anisotropy (e.g., multiple layers with a horizontal axis of symmetry, or a single layer with a dipping axis). When a recording station is located near the boundary of two or more regions with different anisotropy characteristics, the observed splitting parameters are dependent on the location of the ray piercing points. Such a piercing-point dependence is clearly observed using a total of 360 pairs of XKS splitting parameters at three stations situated near the northeastern edge of the Sichuan Basin in central China. For a given station, the fast orientations differ as much as 90° , and the azimuthal variation of the fast orientations lacks a 90° or 180° periodicity which is expected for double-layered or dipping axis anisotropy. The observed splitting parameters from the three stations are

spatially most consistent when they are projected at a depth of ~ 250 km, and can be explained by shear strain associated with the absolute plate motion and mantle flow deflected by the cone-shaped lithospheric root of the Sichuan Basin.

1. INTRODUCTION

Numerous observational and laboratory studies over the past several decades have suggested that the azimuthal dependence of seismic wave-speed, that is azimuthal anisotropy, is a nearly ubiquitous property of the Earth's upper mantle (e.g., Hess, 1964; Francis, 1969; Leven et al., 1981; Mainprice & Nicolas, 1989; Silver & Chan, 1991; Gao et al., 1994; Savage, 1999; Long & Silver, 2008, 2009; Yang et al., 2017). One of the most commonly used techniques to investigate azimuthal anisotropy is shear wave splitting (SWS) analysis (Fuchs, 1977; Ando et al., 1983; Silver & Chan, 1991; Vinnik et al., 1992; Silver, 1996; Savage, 1999; Long & Silver, 2009). Numerous theoretical and observational studies demonstrate that when a shear wave propagates through a transversely isotropic medium, it splits into two quasi-shear waves with orthogonal polarization orientations propagating at different wave-speeds (Silver, 1996; Savage, 1999; Long & Silver, 2009). The orientation and the strength of the anisotropy for a transversely isotropic medium are quantified by two splitting parameters, the polarization orientation of the fast wave (ϕ or fast orientation) and the delay time between the fast and slow waves (δt or splitting time). The most frequently employed seismic phases for SWS analysis are SKS, SKKS and PKS (hereafter referred to as XKS collectively), which are P-to-S converted waves at the core–mantle boundary on the receiver side (Ando et al.,

1980; Silver & Chan, 1991). Due to the steep angle of incidence of the XKS phases, the resulting splitting parameters possess high lateral resolution but low vertical resolution.

While the splitting parameters measured at a given station can usually be determined reliably, the interpretation of the observed splitting parameters is less trivial and frequently debated (e.g., Gao et al., 2010). Laboratory and geodynamic modelling investigations suggest that strain-induced lattice preferred orientation (LPO) of anisotropic minerals (principally olivine) is mostly responsible for mantle azimuthal anisotropy (Zhang & Karato, 1995). Specifically, in the upper asthenosphere, simple shear strain induced by the relative movement between the lithosphere and asthenosphere tends to align the a-axis of olivine subparallel to the relative movement direction between the two rheologically contrasting layers (Ben Ismail & Mainprice, 1998; Long & Silver, 2009; Ohuchi & Irifune, 2013), while anisotropy of the lithosphere is generally related to vertically coherent deformation caused by horizontal compression, with the fast orientation being perpendicular to the maximum horizontal shortening direction (Silver & Chan, 1991; Silver, 1996; Fouch & Rondenay, 2006). As a result of the non-uniqueness of the LPO-forming processes, the geodynamic implication of SWS observations for a given area is usually ambiguous. Therefore, exploring effective approaches for elucidating anisotropy-forming mechanisms is essential, not only for understanding the origin of seismic anisotropy but also for characterizing past or current deformational processes in the mantle.

The vast majority of the previous SWS studies measure and interpret the splitting parameters based on the assumption of simple anisotropy, which is characterized by a single layer of azimuthal anisotropy with a horizontal axis of symmetry (Silver & Savage,

1994). In this ideal and frequently observed scenario, the anisotropic properties can be objectively reflected by the station-averaged splitting parameters because the individual splitting parameters do not vary with the back azimuth (arriving azimuth or BAZ) of the events. Any significant departure from the simple anisotropy characteristics can result in complex anisotropy. For most complex anisotropy cases, the observed splitting parameters are systematic functions of the BAZ of the seismic events (Silver & Savage, 1994; Rumpker & Silver, 1998). The most common form of complex anisotropy adopted is the two-layer model, which is composed of two anisotropic layers with non-parallel and non-orthogonal horizontal axes of symmetry. The individual splitting parameters in a two-layer model vary systematically against the BAZ, with a period of 90° (Silver & Savage, 1994).

Besides complex anisotropy, another anisotropic structure that can result in azimuthal variation of the splitting parameters is piercing-point-dependent anisotropy. This type of anisotropy can be found when a recording station is situated near the boundary between two or more regions of simple anisotropy with different anisotropic characteristics (Liu & Gao, 2013). The observed fast orientations and/or splitting times at the station vary as functions of ray piercing locations. Similar to complex anisotropy, station-averaged splitting parameters obtained in areas with piercing-point-dependent simple anisotropy cannot objectively represent the actual anisotropic properties. One excellent example of this type of seismic anisotropy is found at Station ENH, which is located in Enshi City, Hubei Province, China (Figure 1). Among the 61 pairs of XKS splitting measurements obtained at this station (Liu & Gao, 2013), the BAZ for 28 pairs is between 111° and 124° , and the fast orientations and splitting times of these

measurements have a mean value of $61.0 \pm 11.0^\circ$ and 0.61 ± 0.17 s, respectively. In comparison, the 33 measurements from events from the west and northwest have mean splitting parameters of $136.6 \pm 15.1^\circ$ and 0.79 ± 0.20 s.

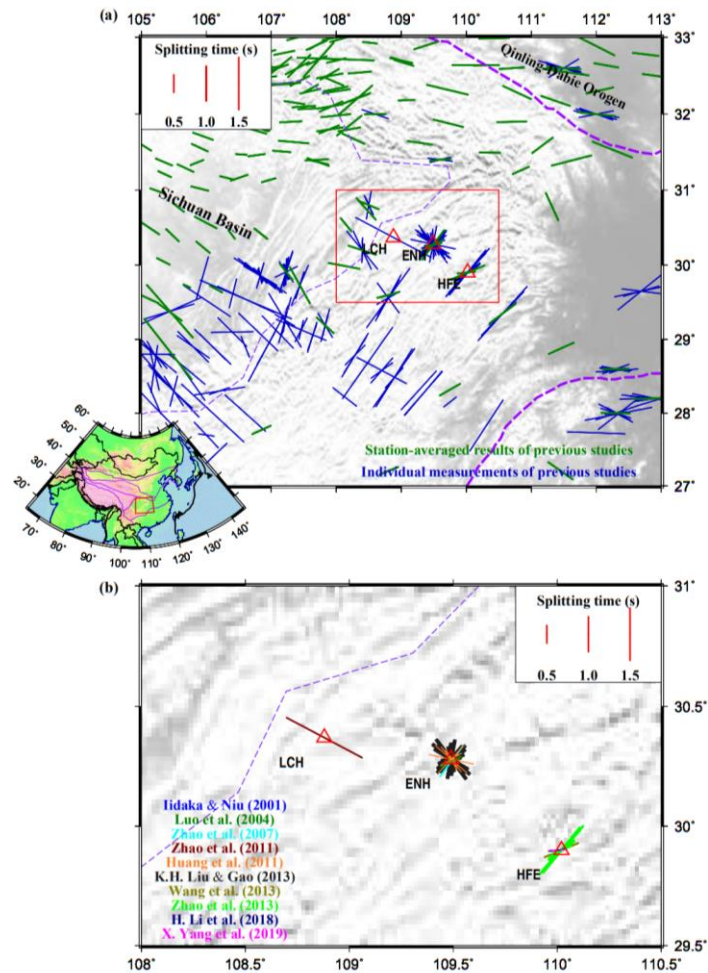


Figure 1. (a) Topographic map of the northeastern part of the Sichuan Basin showing major tectonic boundaries (thick purple dashed lines) and stations used in this study (red triangles with station name). The mapped area is marked by the red rectangle in the inset map of East Asia. The thin purple dashed line presents the boundary of the Sichuan Basin. The thick green and thin blue bars indicate the station-averaged and individual shear-wave splitting (SWS) measurements from different previous studies obtained from <http://www.gm.univ-montp2.fr/splitting/DB/>. (b) Previous SWS measurements at stations used in this study. Different colors represent different studies.

Some previous SWS studies have also measured SWS parameters at Station ENH and surrounding stations (Figure 1). Almost all of them only used SKS events which were dominantly located in the subduction zone of the western Pacific Ocean with a narrow BAZ range of about 110° – 130° (Iidaka & Niu, 2001; Luo et al., 2004; Zhao et al., 2007, 2011, 2013; Wang et al., 2013; Li et al., 2018; Yang et al., 2019). Consequently, the fast orientations from these studies are dominantly NE–SW or ENE–WSW (Figure 1b). The limited BAZ coverage and the assumption of simple anisotropy led to controversial conclusions about the geodynamic implications of the splitting measurements among the previous studies. In this study, we conduct a systematic analysis using an updated data set from ENH and data from two nearby stations to systematically investigate piercing-point-dependent anisotropy and to estimate the depth of the source of the observed anisotropy by utilizing the piercing-point dependence of the splitting parameters.

2. DATA AND METHODS

The teleseismic seismic data set used in this study was recorded by three permanent broad-band stations, locate between 108.0° E– 110.5° E and 29.5° N– 31.0° N (Figure 1). Data from station ENH were obtained from the Incorporated Research Institutions for Seismology (IRIS) Data Management Center (DMC), recorded over a 27-yr period from, 1992 to, 2019, and those from stations HFE and LCH were obtained from the Data Management Centre of China National Seismic Network at the Institute of

Geophysics, China Earthquake Administration, with a recording duration spanning from July 2007 to September 2019 (Zheng et al., 2010).

The splitting parameters are measured and ranked using the procedure detailed in Liu et al. (2008) and Liu & Gao (2013), which is based on the method of minimization of the transverse energy technique (Silver & Chan, 1991). The epicentral distance ranges used for data requesting are 120° – 180° , 95° – 180° and 84° – 180° for PKS, SKKS and SKS, respectively. The minimum cut-off magnitude of the seismograms is 5.6 for events shallower than 100 km, and 5.5 for deeper events (Liu & Gao, 2013). All the seismograms are initially bandpass filtered with corner frequencies of 0.04 and 0.5 Hz to enhance the signal-to-noise ratio (S/R) in the XKS phases. The beginning and the ending times of the XKS window are initially set as $T_{XKS} - 5.0$ s and $T_{XKS} + 20$ s, where T_{XKS} is the theoretical arrival time of the XKS phase computed using the IASP91 Earth model (Kennett & Engdahl, 1991).

Following an S/N based ranking algorithm (Liu et al., 2008), the processed measurements are classified into four ranks as A (outstanding), B (good), C (bad) and N (null, for which XKS energy is only observed on the radial component but not on the transverse component). The splitting parameters, including the fast orientation (ϕ) and splitting time (δt), are initially determined automatically. Subsequently, the quality ranking, the beginning and ending times of the XKS window, and the bandpass filtering frequencies are visually verified and manually adjusted when necessary. In total, 289 teleseismic events are found to have resulted in at least one well-defined (A or B ranking) SWS measurement after the manual checking (Figure 2a). Figure 3 shows examples of quality ‘A’ measurements, which demonstrate significant BAZ dependence of the

splitting parameters obtained at the same stations. The uncertainties in the individual measurements are estimated using the F-test approach specified in Silver & Chan (1991) and represent one standard deviation. The mean splitting time and its uncertainty at a given station or a given area are estimated using the arithmetic average and its standard deviation over all the individual measurements, and the mean fast orientation and its uncertainty are computed using the circular mean and circular standard deviation (Mardia & Jupp, 2000; Gao et al., 2008).

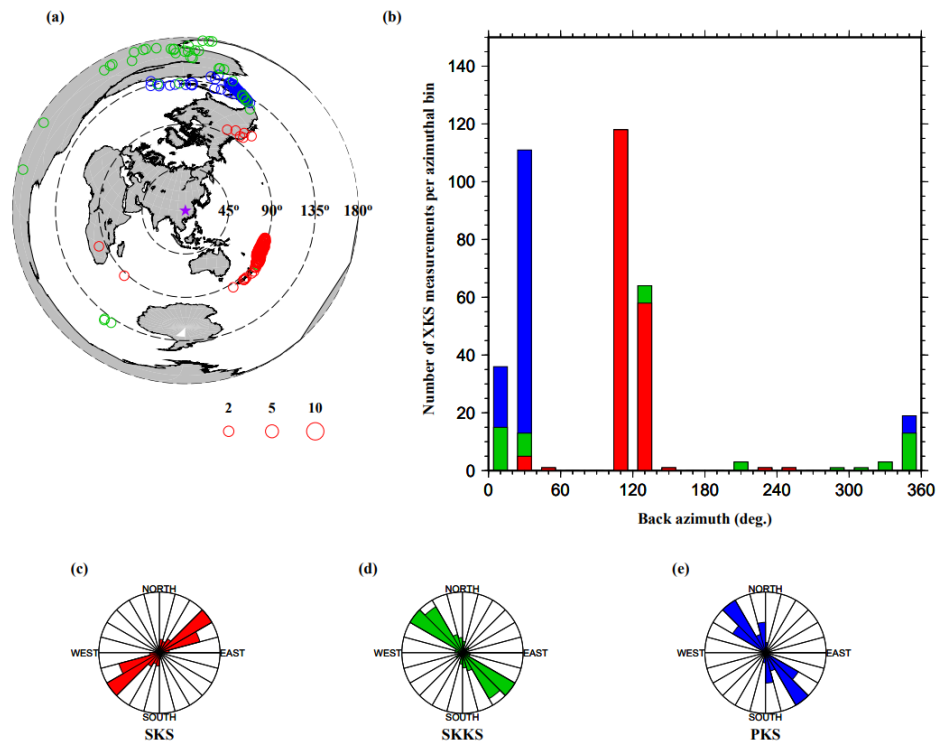


Figure 2. Events location. (a) An azimuthal equidistant projection map showing the spatial distribution of the earthquakes (circles) centered at the study area (purple star). The radius of the circles is proportional to the number of Quality A or B SWS measurements from the events. (b) A histogram of the back azimuthal distribution measured by the SWS measurements. (c–e) Rose diagrams illustrating the fast orientations of the SKS, SKKS, and PKS phases. For all the plots, red, green, and blue colors represent the SKS, SKKS, and PKS events or measurements.

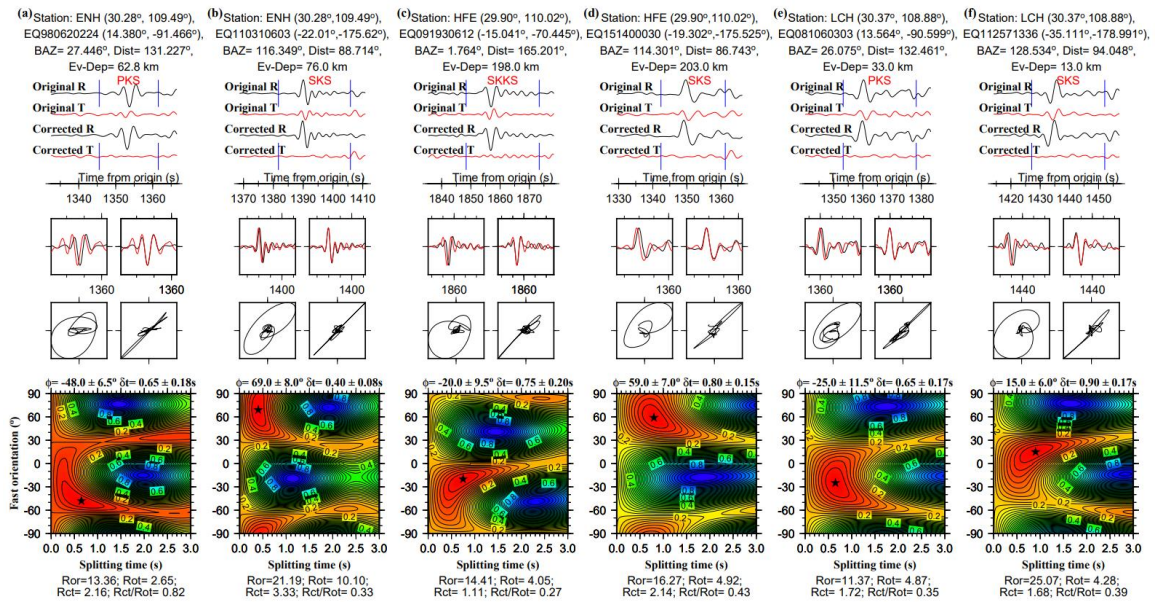


Figure 3. Examples of SWS measurements (quality A) recorded by stations ENH, HFE, and LCH. The plots in the top row show original and corrected radial and transverse components, and the plots in the central rows show the uncorrected and corrected particle motions of the fast and slow particles. The bottom plots are misfit maps, with the color representing the energy on the corrected transverse component. The optimal pair of splitting parameters correspond to the minimum value on the misfit map and are indicated by the star.

3. RESULTS AND COMPARISON WITH MEASUREMENTS FROM PREVIOUS STUDIES

A total of 360 pairs of well-defined splitting measurements were obtained, including, 191 from Station ENH (Figure 4), 78 from HFE (Figure 5) and 91 from LCH (Figure 6). Among those measurements, 125 are from PKS, 50 are from SKKS and 185 are from SKS (Supporting Information Table S1). As shown in Figures 2(a) and (b), most of the SKS events have a BAZ ranging from 100° to 140° and are located in the western Pacific subduction zones. The PKS measurements are mostly from events with a BAZ in the range of 5° – 35° , and the SKKS measurements have two main BAZ ranges which are

$0^\circ\text{--}35^\circ$ and $300^\circ\text{--}360^\circ$. Both the PKS and SKKS events are from the west coast of Central and South America (Figure 2a), and including these non-SKS phases significantly improves the back azimuthal coverage of the SWS measurements. Because a large quantity of well-defined splitting parameters are observed at all the three stations, null measurements, which are characterized by a lack of observable energy on the transverse component, will not be discussed in this study.

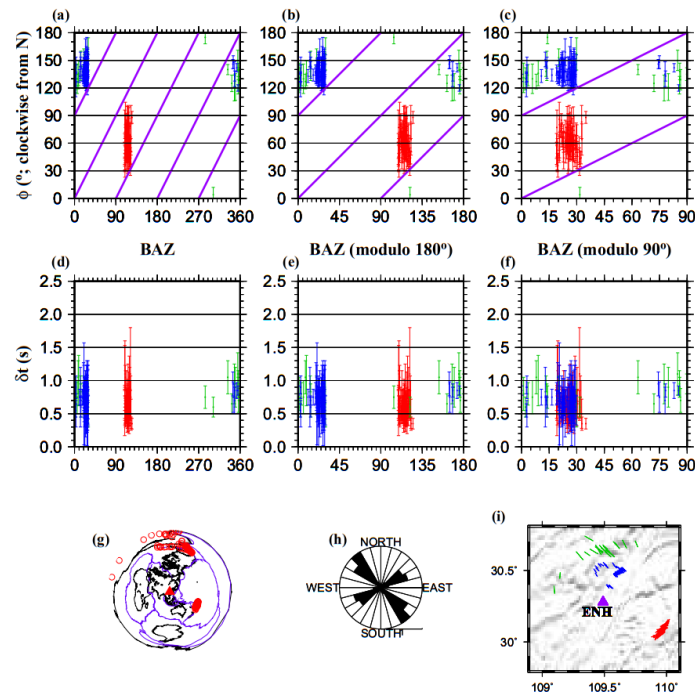


Figure 4. Summary of measurements at Station ENH. (a) Azimuthal variations of the fast orientation plotted against back azimuth; (b) Same as (a) but for the modulo- 180° back azimuth; (c) Same as (a) but for the modulo- 90° back azimuth. The purple lines in (a-c) show $\phi = n \cdot 90 + \text{BAZ}$, where $n = -3, -2, -1, 0, 1$, along which the fast orientation is parallel or orthogonal to the BAZ and thus well-defined measurements are non-existent for simple anisotropy; (d-f) same as (a-c) but for splitting times; (g) an azimuthal equidistant projection map showing events used (circles); (h) a rose diagram showing the distribution of the measured fast orientations; (i) splitting parameters plotted above ray-piercing points at 200 km depth. The triangle represents the station. For all the plots, red, green, and blue colors represent the SKS, SKKS, and PKS events or measurements.

Table 1. SWS measurements from previous and the present studies.

Station	Phase	ϕ (°)	σ_ϕ (°)	δt (s)	$\sigma_{\delta t}$ (s)	N	Reference
ENH	SKS	75.6	7.4	0.36	0.13	7	Iidaka & Niu 2001
	SKS	63.0	14.6	0.60	0.01	12	Luo <i>et al.</i> 2004
	SKS	37.0	-	1.05	-	10	Zhao <i>et al.</i> 2007
	XKS	155.7	52.0	0.73	0.40	10	Huang <i>et al.</i> 2011
	SKS	77.2	4.8	0.45	0.01	22	Wang <i>et al.</i> 2013
	XKS	104.3	49.3	0.71	0.20	61	K.H. Liu & Gao 2013
	SKS	61.0	11.0	0.61	0.17	28	K.H. Liu & Gao 2013
	SKKS	143.9	26.9	0.88	0.21	11	K.H. Liu & Gao 2013
	PKS	134.2	4.1	0.75	0.18	22	K.H. Liu & Gao 2013
	XKS	110.8	48.4	0.67	0.18	191	This study
	SKS	61.4	13.0	0.60	0.17	88	This study
	SKKS	137.8	16.1	0.84	0.16	21	This study
	PKS	137.5	7.1	0.70	0.14	82	This study
	HFE	SKS	67.3	2.1	1.03	0.10	7
SKS		47.2	8.6	1.26	0.13	11	Zhao <i>et al.</i> 2013
SKS		83.7	-	0.48	-	1	H. Li <i>et al.</i> 2018
SKS		85.5	-	0.50	-	1	X. Yang <i>et al.</i> 2019
XKS		55.9	32.6	0.93	0.29	78	This study
SKS		52.4	13.2	1.00	0.28	57	This study
SKKS		125.4	27.7	0.73	0.21	19	This study
PKS		173.5	8.6	0.80	0.21	2	This study
LCH		SKS	128.0	-	2.54	-	1
	XKS	178.2	17.0	0.78	0.18	91	This study
	SKS	9.7	14.9	0.73	0.21	40	This study
	SKKS	167.8	23.6	0.78	0.12	10	This study
	PKS	169.9	8.7	0.83	0.13	41	This study

3.1. STATION ENH

The 191 measurements obtained at Station ENH have a mean δt of 0.67 ± 0.18 s and a mean ϕ of $110.8 \pm 48.4^\circ$, ranging from 0.35 to 1.15 s and 4° to 175° , respectively.

The SKS events record by station ENH mostly come from the western Pacific subduction

zones in an approximately 110° – 125° BAZ range with dominantly ENE–WSW fast orientations. The PKS and SKKS events are mainly from the west coast of Central and South America in the BAZ ranges of 0 – 40° and 340 – 360° with mostly NW-SE fast orientations (Figure 4). When the fast orientations are plotted in the modulo 90° BAZ domain, two distinct groups of measurements are found in the BAZ (modulo- 90°) range of 15 – 30° (Figure 4c). Those in the first group are mostly SKS measurements and the fast orientations are in the range of 36 – 92° , and those in the second group are SKKS or PKS measurements with fast orientations from about 120° to nearly N–S. The apparent azimuthal variation is inconsistent with a multiple layered anisotropic structure which is characterized by a systematic azimuthal variation with a 90° periodicity (Silver & Savage, 1994; Rumpker & Silver, 1998), that is in a modulo- 90° domain, the splitting parameters are expected to have similar values for a given BAZ.

Several studies have measured shear wave splitting at this station, as summarized in Table 1. The number of individual measurements obtained by the studies ranges from 7 to 61 (while this study obtained 191 measurements). Except for Huang et al. (2011) which uses SKS, SKKS, PKS and SKiKS, and Liu & Gao (2013) which uses XKS, to our knowledge, all the other studies only use the SKS phase. The station averaged fast orientations for these previous studies (Iidaka & Niu, 2001; Luo et al., 2004; Wang et al., 2013) are between 37° and 77° which is comparable to the value of 61° from this study when only the SKS phase is used and are significantly different from results obtained using PKS and SKKS (about 138°). On the other hand, results from each of the three XKS phases obtained in our study are statistically consistent with the corresponding values reported by Liu & Gao (2013) (Table 1). Those comparisons suggest that only

using a single phase could result in misleading results. In addition, station averages are heavily dependent on the relative proportion of the events from the different BAZ groups, and thus do not objectively reflect the true anisotropy characteristics beneath this station.

3.2. STATION HFE

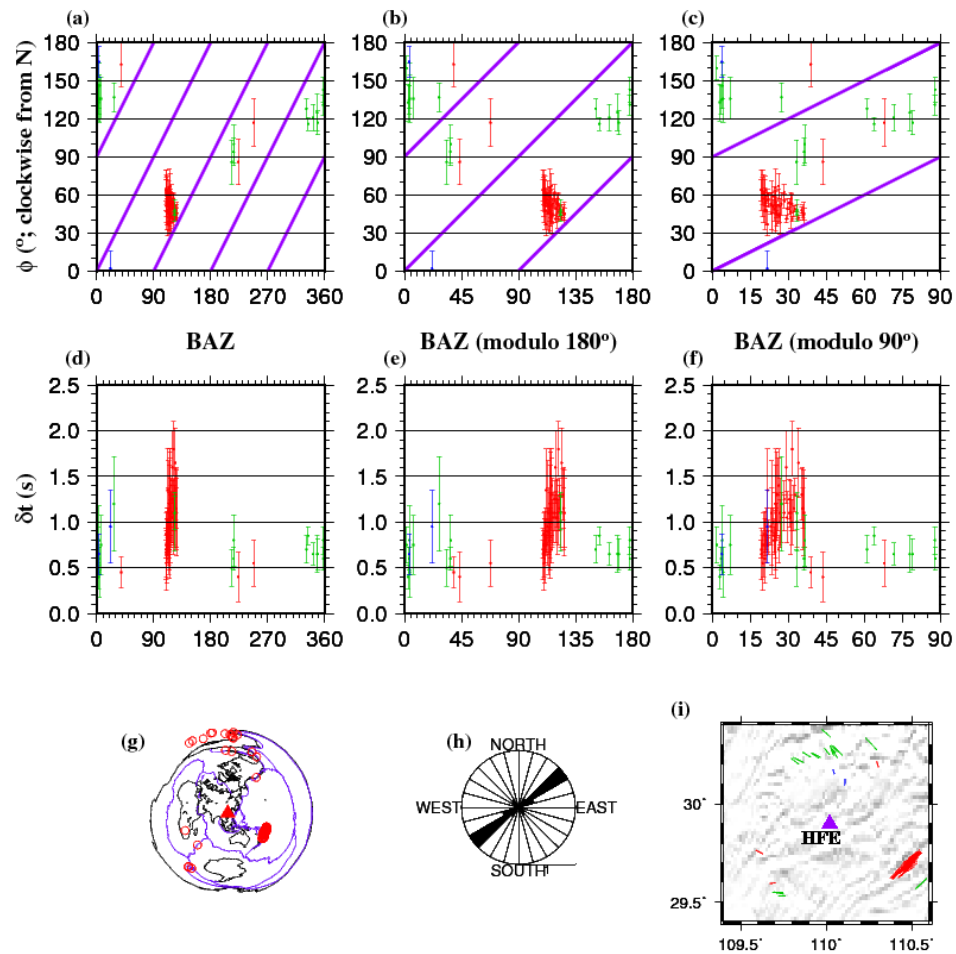


Figure 5. Same as Figure 4 but for Station HFE.

The 78 events recorded by Station HFE resulted in a mean δt of 0.93 ± 0.29 s and a mean ϕ of $55.9 \pm 32.6^\circ$ (Figure 5). The PKS and SKKS measurements are mainly from

BAZ ranges of $0\text{--}15^\circ$ and $330\text{--}360^\circ$, and the resulting fast orientations are dominantly NW–SE. In contrast, the SKS measurements are mostly from events in the BAZ range spanning from 110° to 130° and the fast orientations are mostly NE–SW. A group of five measurements from events in the SW quadrant demonstrate mostly E–W fast orientations (Figure 5i). Similar to ENH, the azimuthal variations are inconsistent with a multiple layered anisotropic structure (Figure 5c).

Previous studies conducted at this station (Wang et al., 2013; Zhao et al., 2013; Li et al., 2018; Yang et al., 2019) all used the SKS phase, and the number of measurements ranges from 1 to 11 comparing to 78 obtained by this study. The fast orientations from the previous studies range from 47° to 86° , while the splitting times are between 0.48 and 1.26 s. Similar to ENH, our SKS fast orientation (52°) is comparable to results from the previous SKS splitting measurements, but significantly different fast orientations with those obtained by previous studies are found when PKS and SKKS are used.

3.3. STATION LCH

The 91 pairs of measurements from LCH have dominantly N–S fast orientations with a mean value of $178.2 \pm 17.0^\circ$, and the resulting δt values range from 0.4 to 1.4 s with a mean of 0.78 ± 0.18 s. The measurements can be divided into two groups based on the BAZ range of the events. The first group, which is mostly composed of SKKS and PKS measurements, has a BAZ in the range of $15\text{--}40^\circ$, and the second group, which are mostly SKS measurements, has a BAZ range between 120° and 140° (Figure 6). For the first group, the mean splitting parameters are $167.3 \pm 11.6^\circ$ for the fast orientation, and

0.85 ± 0.16 s for the splitting time, and for the second group, the corresponding values are $12.8 \pm 10.3^\circ$ and 0.69 ± 0.16 s.

Only one previous study measured SWS at this station (Zhao et al., 2011), which reported a fast orientation of 128° and a splitting time of 2.54 s from a single SKS event. Both the fast orientation and the splitting time are significantly different from results obtained by this study using any of the three phases (Table 1).

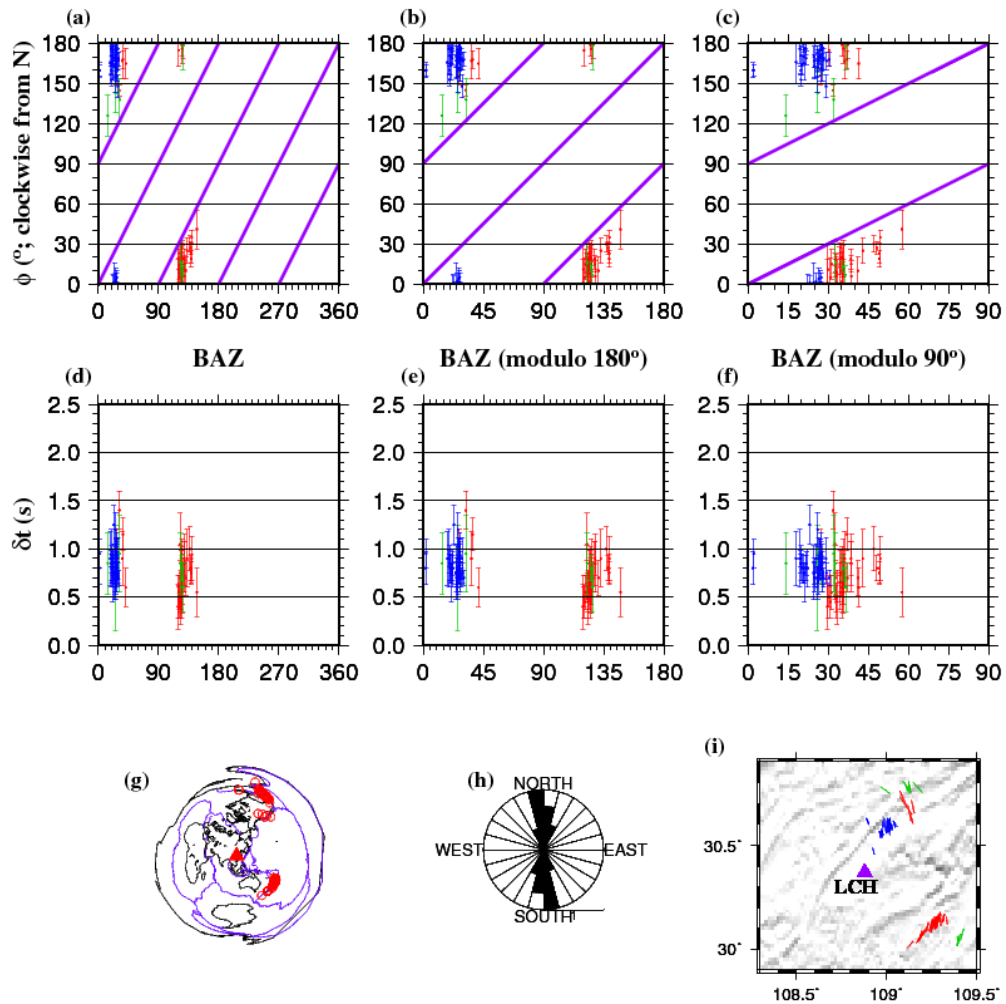


Figure 6. Same as Figure 4 but for Station LCH.

4. DISCUSSION

4.1. EVIDENCE FOR PIERCING-POINT-DEPENDENT ANISOTROPY

The clear dependence of the splitting parameters on the arriving azimuth of the XKS events adequately indicates that the observed splitting parameters cannot be readily explained by a laterally homogenous single layer of anisotropy with a horizontal axis of symmetry, which is an assumption when the vast majority of previous SWS studies employed for interpreting the measurements. Traditionally, departures from this ideal model are termed as complex anisotropy (Silver & Savage, 1994), and the most commonly observed complex anisotropy is composed of two or more layers with horizontal but non-parallel and non-orthogonal axes of symmetry. These multiple layers of anisotropy are characterized by a systematic azimuthal variation of both the ϕ and δt observations, typically possessing a 90° periodicity (Rumpker & Silver, 1998), which is not observed at any of the three stations (Figures 4–6). Additionally, for multiple layered anisotropy, some of the ϕ values can be approximately parallel or orthogonal to the BAZ (Liu & Gao, 2013), which are also not observed (Figures 4–6). Therefore, the observed apparent azimuthal variations of the splitting parameters cannot be reliably attributed to multilayered anisotropy.

Relative to two-layered anisotropy, a less commonly observed form of complex anisotropy is constituted by a single layer with a dipping axis of symmetry (Levin & Park, 1997; Levin et al., 2007), which is characterized by a systematic azimuthal variation of the splitting parameters with a 180° periodicity. Even though the azimuthal distribution of the XKS events is limited at some of the stations, it is clear that a 180°

periodicity is absent at all the three stations (Figures 4b, 5b and 6b). Compared with multilayered or dipping axis models, a more viable scenario is spatially varying simple anisotropy. In addition to the lack of 90° or 180° periodicity, the strongest evidence for this model is from the fact that when the observed splitting parameters are projected at a certain depth, a spatially coherent pattern is observed, as detailed in the next section.

4.2. ANISOTROPY DEPTH ESTIMATION

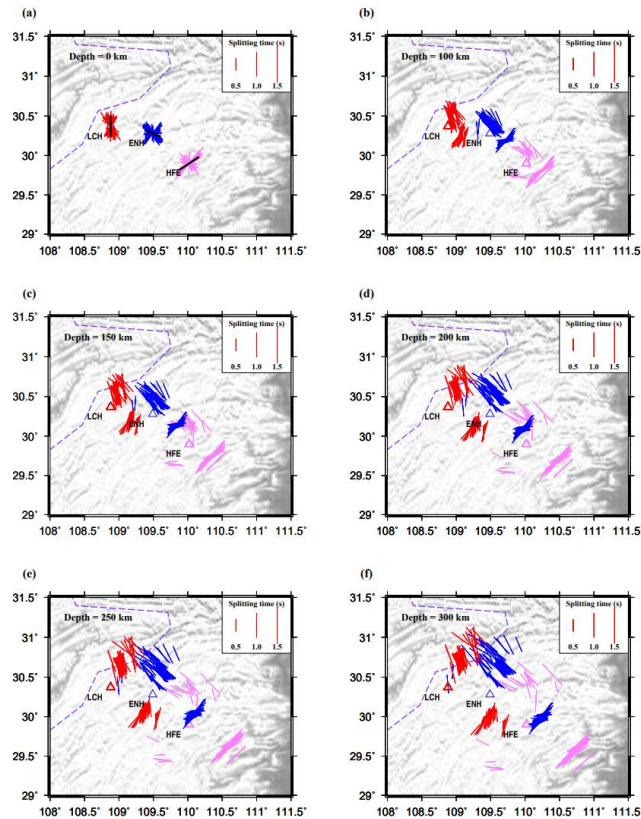


Figure 7. PKS, SKKS, and SKS splitting parameters (quality A and B) from this study plotted at piercing point locations at different depths. The depth values are shown in the upper left corner. The black bars in (a) are the station averaged SWS parameters, and the red, blue, and pink bars indicate individual measurements from stations LCH, ENH, and HFE, respectively.

We next project the splitting measurements to different depths and explore the spatial consistency of the splitting parameters. With increasing depth, the piercing points of the XKS rays recorded by the stations spread away from the stations and eventually overlap (Figure 7). As the assumed depth approaches ~ 250 km, measurements with nearby piercing points show the highest similarity to each other (Figure 7e) and can be approximately divided into three groups. Those in the group north of 30.2° N latitude have a dominantly NW-SE fast orientation, those in the south-central part of the study area are mostly E-W oriented, and the rest measurements have mostly NE-SW fast orientations. The spatial coherency appears to decrease at greater depth (Figure 7f).

We use two approaches, which are identical in principle but different in visual display and vertical sampling intervals, to quantify the initial observation that the spatial coherency of the splitting parameters vary with the assumed depth, and to locate the optimal depth with the highest spatial coherency. For the first approach, we divide the study area into overlapping circles with a 0.2° radius and 0.2° distance between the neighboring circles. For each depth, we calculate the sample standard deviation (SD) of the fast orientations within each of the circles and then get the average of SD value for each of the depths of 0, 100, 150, 200, 250, 300 and 350 km. A circle is not employed if the number of splitting measurements in it is one or less. The results show that the lowest averaged SD value is found at 250 km (Figure 8e). For the second approach, we apply the spatial coherency method first proposed in Gao et al. (2010). This technique employs the idea that the observed splitting parameters will reach the highest spatial coherency if the assumed anisotropy depth is correct (see Liu & Gao, 2011; Gao & Liu, 2012 for the detailed descriptions). The conditions for the technique to be reliably applied, including

adequate BAZ coverage, densely spaced (e.g., 70 km or less) stations, and spatially varying simple anisotropy, can all be satisfied in this study area. The resulting F_v , which is a dimensionless factor reflecting the spatial variation of the measurements as a function of the assumed depth of anisotropy, shows a clear minimum at the depth of 250 km (Figure 8h), a conclusion that is consistent with results from the previous approach. The actual thickness of the anisotropic layer is dependent on the anisotropy amplitude. Under the assumption that the layer has a mean anisotropy of 4 per cent (Mainprice & Silver, 1993), a splitting time of 0.75 s corresponds to a thickness of ~ 80 km.

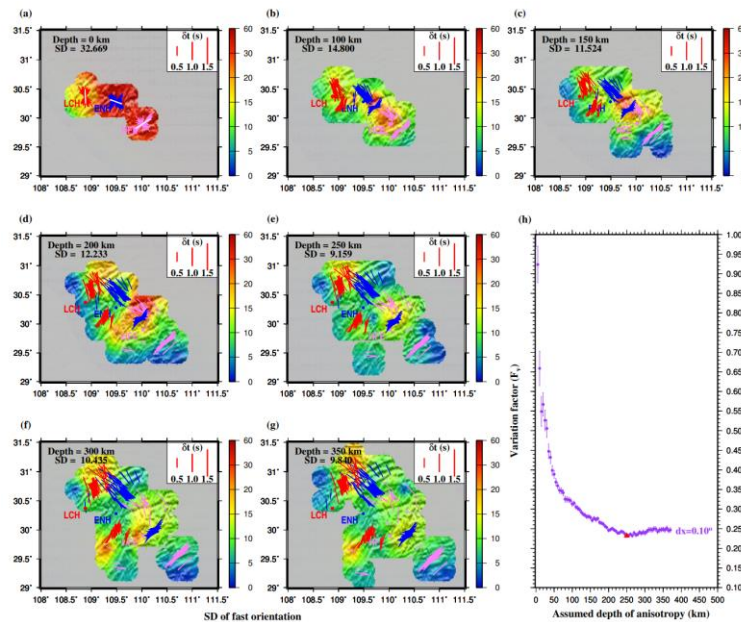


Figure 8. (a–g) Distribution of the standard deviation (SD) of spatially averaged fast orientations in 0.2° radius circles at the depth of 0, 100, 150, 200, 250, 300, and 350 km. The averaged SD results are indicated in the upper left corner of each map. The results plotted were resampled into a resolution of 0.1° . The red, blue, and pink bars indicate individual measurements of stations LCH, ENH, and HFE, respectively. (h) Anisotropy depth analysis for the SWS measurements based on the spatial coherence technique (K.H. Liu & Gao 2011), resulting in an optimal depth of anisotropy at 250 km. The red triangle on the curve marks the depth with the minimum variation factor.

4.3. SYNTHETIC TEST

Like it is routinely assumed by the vast majority of SWS studies, the above analysis and interpretation of the SWS measurements were made based on the ray theory, that is the measurements only reflect physical properties along the geometric ray paths. In reality, due to the finite frequencies of the XKS waves, the splitting measurements are functions of anisotropy primarily in the first Fresnel zone (Alsina & Snieder, 1995; Chevrot, 2006). For a shear wave with a dominant frequency of 0.15 Hz, the radius of the first Fresnel zone at 250 km depth is about 60 km. As shown in Figures 2(a) and (b), most of the events used in the study are from either the north or the southeast. For a given station, the Fresnel zones of the XKS waves from the two groups overlap significantly at shallow depth (e.g., < 100 km), and the amount of overlapping decreases at greater depths (see Figure 9b for an example for Station ENH). At the optimal depth of 250 km, the overlapping area is merely 13 per cent of the area of the first Fresnel zone, suggesting that at this (and greater) depth, the two groups of events recorded by the same station sample different regions.

To test if a sharp E–W boundary separating the two regions of anisotropy can indeed produce the observed pattern of splitting parameters, we used the SPECFEM3D GLOBE package (Komatitsch & Vilotte, 1998; Komatitsch & Tromp, 1999) to produce synthetic seismograms. Ideally, given the large ($\sim 83^\circ$ – 180°) epicentral distances for the XKS waves, a global-scale simulation with a realistic 3-D structure should be used for simulating wave propagation. However, in order to achieve frequencies that are high enough to match those of the XKS waves, the computational cost for a global scale

simulation is unrealistically high at the present time, and is actually not essential for our purpose, as demonstrated below.

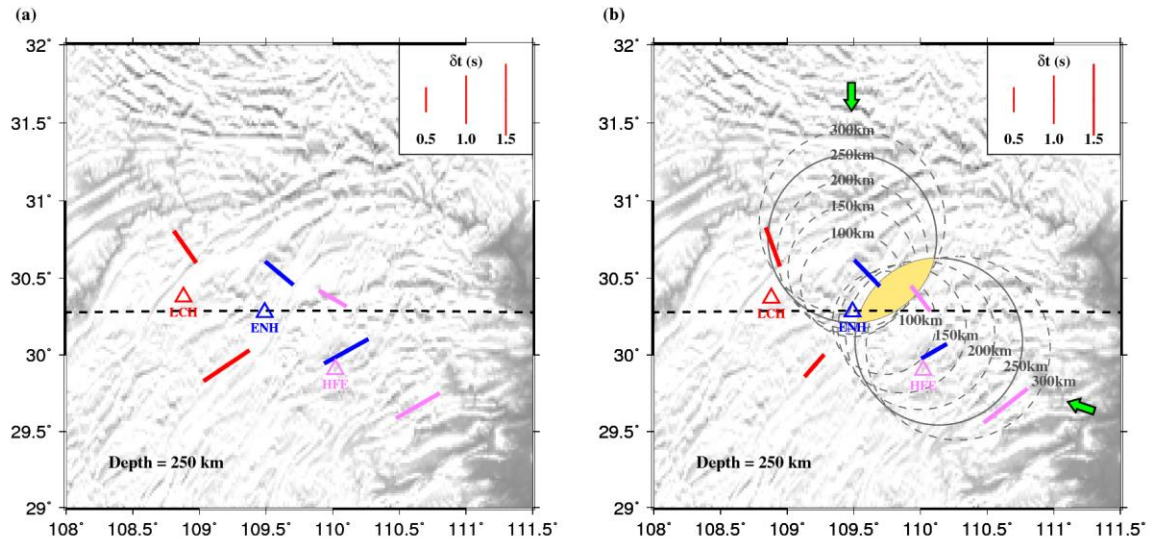


Figure 9. Comparison of SWS measurements using synthetic seismograms generated using SPEC3D_GLOBE (a) and those from corresponding observed seismograms (b). For each station (triangles), the splitting parameters (bars) from an event from north and another event from southeast are measured and are plotted at the 250 km depth piercing points using the same color as the station. The circles in (b) are the first Fresnel zones from two events (whose back azimuths are marked by the green arrows) recorded by Station ENH at various depth. The solid circles are the Fresnel zones at 250 km depth. The E-W dashed line approximately separates two regions of anisotropy with different fast orientations.

We constructed a regional model with a depth range of 0–950 km and a surface area of 10° by 10° centered at station ENH. The model has 256 surface spectral elements and is capable of producing synthetic seismograms for periods longer than ~ 1.9 s which is comparable to the dominant period of the XKS waves used in the study. The transversely isotropic version of the spherically symmetric Preliminary Reference Earth Model (PREM; Dziewonski & Anderson, 1981) was used as the background model, and

an azimuthally anisotropic layer at the depth range of, 200–280 km was introduced based on the estimated optimal depth and layer thickness. The fast orientation and splitting time of the layer for the area north of Station ENH were set as -30° and 0.8 s, respectively, and those in the area south of the station were set as 60° and 0.8 s, respectively. For each of the three stations, an event from the northern group and another event from the SE group were chosen for the simulation. Because the source must reside inside the volume, a local event was placed at the piercing point of the corresponding XKS ray path at 500 km depth. As the initial polarization orientation of the shear wave from a local event is dependent on the focal mechanism, the technique of minimizing the lesser of the two eigenvalues of the covariance matrix of the seismograms (Silver & Chan, 1991) is used to simultaneously search for the initial polarization and the splitting parameters. Figure 10 shows example synthetic seismograms and their splitting analyses. A comparison of the resulting splitting parameters computed from the synthetic and observed seismograms (Figure 9 and Supporting Information Table S2) suggests a simple model with two uniform regions of anisotropy and a sharp vertical boundary can explain the major characteristics of the SWS measurements reasonably well.

4.4. GEODYNAMIC IMPLICATIONS

Previous studies suggest that the lithospheric thickness beneath the study area is between ~ 200 and 250 km (Wang et al., 2013; Pasyanos et al., 2014; Shan et al., 2021), which is comparable to the ~ 250 km resultant optimal depth of anisotropy (Figure 8h). We thus speculate that the anisotropy observed beneath the three stations mainly comes from the upper asthenosphere, in the rheological transition zone between the lithosphere

and the asthenosphere. This conclusion is consistent with the result of numerous previous seismic anisotropy studies proposing that mantle flow plays an important role in the formation of seismic anisotropy beneath central China and its adjacent areas (e.g., Bai et al., 2009; Huang et al., 2011, 2015; Li et al., 2011; Kong et al., 2018), probably from the westward subduction of the Pacific plate, mantle flow associated with absolute plate motion (APM) of the Eurasian Plate (e.g., Huang et al., 2011) or with India–Eurasia collision (e.g., Bai et al., 2009; Li et al., 2011; Huang et al., 2015; Kong et al., 2018; Liu et al., 2019).

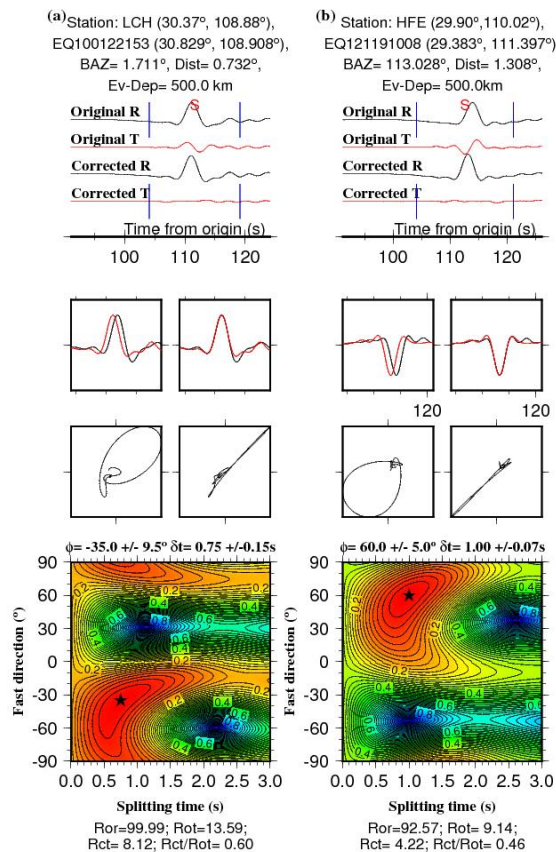


Figure 10. Same as Figure 3 but for the SWS measurements computed from the synthetic seismograms for two station-event pairs.

The bottom of the thick lithosphere of the Sichuan Basin (SCB) is revealed to have a downward cone shape by some previous seismic tomographic studies (e.g., Pasyanos et al., 2014; Bao et al., 2015; Van der Meer et al., 2018; Shan et al., 2021). The SWS measurements we obtained in this study have two dominant fast orientations and are spatially clustered when they are projected to the optimal depth of 250 km, approximately separated by the latitude of station ENH (Figure 8e). The fast orientations in the northern group are approximately consistent with the APM direction, and those in the southern group are subparallel to the strike of the margin of the lithospheric root of the SCB in the area (NE–SW). These observations can be explained by a simple mantle flow model that consists of both APM-induced and root-deflected mantle flow systems (Figure 11), similar to what has been proposed for other areas with large lateral variations in lithospheric thickness such as the southern and eastern edges of the North American craton (Fouch et al., 2000; Refayee et al., 2014; Yang et al., 2014, 2017). Under this model, the NW–SE fast orientations in the northern area reflect APM-induced anisotropy or a combination of APM-induced anisotropy and anisotropy associated with a flow field moving around the northern edge of the thick lithospheric block, while the NE–SW oriented anisotropy observed in the southern area, which is inconsistent with the APM direction, is associated with the flow system deflected by the eastern edge of the thick lithospheric block beneath the SCB. The proposed model provides a viable explanation for the puzzling observation that around the NE corner of the SCB, the fast orientations are different from those observed in the surrounding areas (Figure 1). This model can also explain most previous SWS measurements in the vicinity of the SCB, especially those in its peripheral areas (Figure 11). The general agreement between the observed fast

orientations and those predicted by the mantle flow system inferred from the model implies that to the first order, lithospheric fabric has a less significant contribution than mantle flow to the observed azimuthal anisotropy in the vicinity of the SCB, although a more quantitative evaluation of the contribution from each of the layers cannot be made solely based on SWS measurements presented in this study. The dominantly sublithospheric origin of the observed anisotropy is also hinted by the estimated depth of the source of anisotropy based on the spatial coherency analysis, and the fact that events from different azimuthal recorded by the same station show different splitting parameters (Alsina & Snieder, 1995).

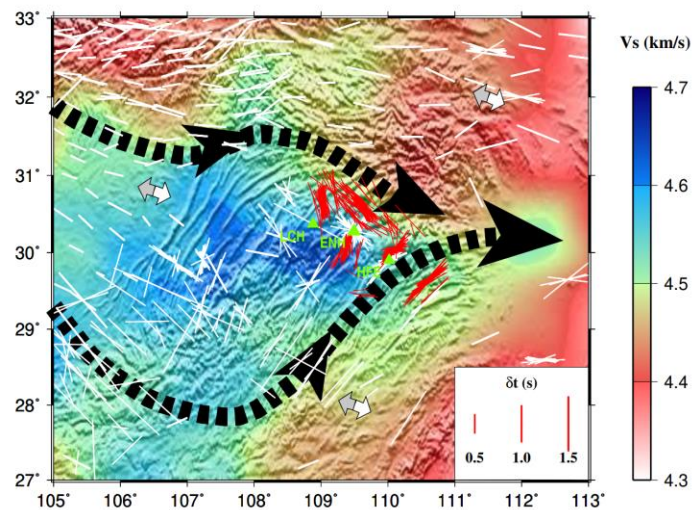


Figure 11. A schematic model showing the mantle flow field beneath the study area. The white and red bars are SWS measurements from previous studies and this study, respectively. The black dashed lines with arrows indicate the direction of mantle flow deflected by the keel of the thick lithosphere keel beneath the SCB. The background color denotes shear wave velocities at the depth of 160 km (Bao *et al.* 2015). The gray and white arrows represent the APM directions computed using the HS3-NUVEL-1A model (Gripp & Gordon 2002) and the NNR-MORVEL56 model (Argus *et al.* 2011), respectively.

5. CONCLUSIONS

The SWS measurements observed at three stations situated near the NE margin of the SCB exhibit systematic azimuthal variations in the fast orientations and lack a 90° or 180° periodicity which is expected for the most common forms of complex anisotropy. Spatial coherency analysis of the splitting parameters suggests that the source of anisotropy beneath the study area mostly locates in the depth of ~250 km which is comparable to the depth of the bottom of the seismically determined lithosphere in the area. The observations can be explained by a simple geodynamic model invoking APM-related simple shear in the transitional layer between the partially coupled lithosphere and the asthenosphere, and mantle flow deflected by the thick lithospheric root of the SCB in the upper asthenosphere. This study advocates the consideration of laterally heterogeneous anisotropy structures for the interpretation of splitting measurements.

ACKNOWLEDGMENTS

We thank S. Chevrot, an anonymous reviewer, and the editor I. Bastow for their constructive reviews that significantly improved the manuscript, and X. Bao for providing the velocity model plotted in Figure 11. All the figures were produced using the Generic Mapping Tools (Wessel et al., 2019). This study was partially supported by the U.S. National Science Foundation under awards 1830644 to KL and SG and, 1919789 to SG.

DATA AVAILABILITY

Data used in the study are available from the IRISDMC (<http://ds.iris.edu/ds/nodes/dmc>; last accessed: December 2019) and DataManagement Centre of China National Seismic Network at Institute of Geophysics, China Earthquake Administration (SEISDMC; last accessed: September 2019).

APPENDIX

Supplementary material related to this paper can be found on the website at <https://doi.org/10.1093/gji/ggab285>.

REFERENCES

- Alsina, D. & Snieder, R., 1995. Small-scale sublithospheric continental mantle deformation: Constraints from SKS splitting observations, *Geophys. J. Int.*, **123**, 431–448, doi:10.1111/j.1365-246X.1995.tb06864.x.
- Ando, M., Ishikawa, Y. & Wada, H., 1980. S-wave anisotropy in the upper mantle under a volcanic area in Japan, *Nature*, **286**, 43–46.
- Ando, M., Ishikawa, Y. & Yamazaki, F., 1983. Shear wave polarization anisotropy in the upper mantle beneath Honshu, Japan, *J. Geophys. Res.*, **88**(B7), 5850–5864, doi:10.1029/jb088ib07p05850.
- Argus, D. F., Gordon, R. G. & DeMets, C., 2011. Geologically current motion of 56 plates relative to the no-net-rotation reference frame, *Geochemistry, Geophysics, Geosystems*, **12**(11), doi:10.1029/2011gc003751.

- Bai, L., Iidaka, T., Kawakatsu, H., Morita, Y. & Dzung N., 2009. Upper mantle anisotropy beneath Indochina block and adjacent regions from shear-wave splitting analysis of Vietnam broadband seismograph array data, *Phys. Earth Planet. Inter.*, **176**(1-2), 33–43, doi:10.1016/j.pepi.2009.03.008.
- Ben Ismail, W. & Mainprice, D., 1998. An olivine fabric database: An overview of upper mantle fabrics and seismic anisotropy, *Tectonophysics*, **296**, 145-157, doi:10.1016/S0040-1951(98)00141-3.
- Bao, X., Song, X. & Li, J., 2015. High-resolution lithospheric structure beneath Mainland China from ambient noise and earthquake surface-wave tomography, *Earth Planet. Sci. Lett.*, **417**, 132–14, doi:10.1016/j.epsl.2015.02.024.
- Chevrot, S., 2006. Finite-frequency vectorial tomography: A new method for high-resolution imaging of upper mantle anisotropy, *Geophys. J. Int.*, **165**, 641–657, doi:10.1111/j.1365-246X.2006.02982.x.
- Dziewonski, A. M. & Anderson, D. L., 1981. Preliminary reference Earth model, *Phys. Earth Planet. Inter.*, **25**(4), 297–356, doi:10.1016/0031-9201(81)90046-7.
- Fouch, M. J., Fischer, K. M., Parmentier, E. M., Wysession, M. E. & Clarke, T. J., 2000. Shear wave splitting, continental keels, and patterns of mantle flow, *J. Geophys. Res.*, **105**(B3), 6255–6275, doi:10.1029/1999jb900372.
- Fouch, M. J. & Rondenay, S., 2006. Seismic anisotropy beneath stable continental interiors, *Phys. Earth Planet. Inter.*, **158**(2-4), 292–320, doi:10.1016/j.pepi.2006.03.024.
- Francis, T. J. G., 1969. Generation of Seismic Anisotropy in the Upper Mantle along the Mid-Oceanic Ridges, *Nature*, **221**(5176), 162–165, doi:10.1038/221162b0.
- Fuchs, K., 1977. Seismic anisotropy of the subcrustal lithosphere as evidence for dynamical processes in the upper mantle, *Geophys. J. Int.*, **49**(1), 167–179, doi:10.1111/j.1365-246x.1977.tb03707.x.
- Gao, S., Davis, P. M., Liu, H., Slack, P. D., Zorin, Y. A., Mordvinova, V. V., Kozhevnikov, V.M. & Meyer, R.P., 1994. Seismic anisotropy and mantle flow beneath the Baikal rift zone, *Nature*, **371**(6493), 149, doi:10.1038/371149a0.
- Gao, S. S., Liu, K. H., Stern, R. J., Keller, G. R., Hogan, J. P., Pulliam, J. & Anthony, E. Y., 2008. Characteristics of mantle fabrics beneath the south-central United States: Constraints from shear-wave splitting measurements, *Geosphere*, **4**, 411-417, doi:10.1130/GES00159.1.

- Gao, S. S. & Liu, K. H., 2012. AnisDep: A FORTRAN program for the estimation of the depth of anisotropy using spatial coherency of shear-wave splitting parameters, *Computers & Geosciences*, **49**, 330–333, doi:10.1016/j.cageo.2012.01.020.
- Gao, S. S., Liu, K. H. & Abdelsalam, M. G., 2010. Seismic anisotropy beneath the Afar Depression and adjacent areas: Implications for mantle flow, *J. Geophys. Res.*, **115**(B12), doi:10.1029/2009jb007141.
- Gripp, A. E. & Gordon, R. G., 2002. Young tracks of hotspots and current plate velocities, *Geophys. J. Int.*, **150**, 321–361, doi:10.1046/j.1365-246X.2002.01627.x.
- Hess, H. H., 1964. Seismic Anisotropy of the Uppermost Mantle under Oceans, *Nature*, **203**(4945), 629–631, doi:10.1038/203629a0.
- Huang, Z., Wang, L., Xu, M., Ding, Z., Wu, Y., Wang, P., Mi, N., Yu, D. & Li, H., 2015. Teleseismic shear-wave splitting in SE Tibet: Insight into complex crust and upper-mantle deformation, *Earth Planet. Sci. Lett.*, **432**, 354–362, doi:10.1016/j.epsl.2015.10.027.
- Huang, Z., Wang, L., Zhao, D., Mi, N. & Xu, M., 2011. Seismic anisotropy and mantle dynamics beneath China, *Earth Planet. Sci. Lett.*, **306**(1-2), 105–117, doi:10.1016/j.epsl.2011.03.038.
- Iidaka, T. & Niu, F., 2001. Mantle and crust anisotropy in the eastern China region inferred from waveform splitting of SKS and PpSms, *Earth, Planets and Space*, **53**(3), 159–168, doi:10.1186/bf03352373.
- Kennett, B. L. N. & Engdahl, E. R., 1991. Traveltimes for global earthquake location and phase identification, *Geophys. J. Int.*, **105**(2), 429–465, doi:10.1111/j.1365-246x.1991.tb06724.x.
- Komatitsch, D. & Tromp, J., 1999. Introduction to the spectral element method for three-dimensional seismic wave propagation, *Geophys. J. Int.*, **139**(3), 806–822, doi:10.1046/j.1365-246x.1999.00967.x.
- Komatitsch, D. & Vilotte, J.P., 1998. The spectral-element method: an efficient tool to simulate the seismic response of 2D and 3D geological structures, *Bull. seism. Soc. Am.*, **88**, 368–392.
- Kong, F., Wu, J., Liu, L., Liu, K. H., Song, J., Li, J. & Gao, S. S., 2018. Azimuthal anisotropy and mantle flow underneath the southeastern Tibetan Plateau and northern Indochina Peninsula revealed by shear wave splitting analyses, *Tectonophysics*, **747**, 68–78, doi:10.1016/j.tecto.2018.09.013.

- Leven, J. H., Jackson, I. & Ringwood, A. E., 1981. Upper mantle seismic anisotropy and lithospheric decoupling, *Nature*, **289**(5795), 234–239, doi:10.1038/289234a0.
- Levin, V. & Park, J., 1997. Crustal anisotropy in the Ural Mountains Foredeep from teleseismic receiver functions, *Geophys. Res. Lett.*, **24**(11), 1283–1286, doi:10.1029/97gl51321.
- Levin, V., Okaya, D. & Park, J., 2007. Shear wave birefringence in wedge-shaped anisotropic regions, *Geophys. J. Int.*, **168**(1), 275–286, doi:10.1111/j.1365-246x.2006.03224.x.
- Li, H. et al., 2018. Seismic Imaging of Lithosphere Structure and Upper Mantle Deformation Beneath East-Central China and Their Tectonic Implications, *J. Geophys. Res.*, **123**(4), 2856–2870, doi:10.1002/2017jb014992.
- Li, Y., Wu, Q., Zhang, F., Feng, Q. & Zhang, R., 2011. Seismic anisotropy of the Northeastern Tibetan Plateau from shear wave splitting analysis, *Earth Planet. Sci. Lett.*, **304**(1-2), 147–157, doi:10.1016/j.epsl.2011.01.026.
- Liu, K. H. & Gao, S. S., 2011. Estimation of the Depth of Anisotropy Using Spatial Coherency of Shear-Wave Splitting Parameters, *Bull. Seismol. Soc. Am.*, **101**(5), 2153–2161, doi:10.1785/0120100258.
- Liu, K. H. & Gao, S. S., 2013. Making Reliable Shear-Wave Splitting Measurements, *Bull. Seismol. Soc. Am.*, **103**(5), 2680–2693, doi:10.1785/0120120355.
- Liu, K. H., Gao, S. S., Gao, Y. & Wu, J., 2008. Shear wave splitting and mantle flow associated with the deflected Pacific slab beneath northeast Asia, *J. Geophys. Res.*, **113**(B1), doi:10.1029/2007jb005178.
- Liu, L., Gao, S. S., Liu, K. H., Li, S., Tong, S. & Kong, F., 2019. Toroidal mantle flow induced by slab subduction and rollback beneath the Eastern Himalayan syntaxis and adjacent areas, *Geophys. Res. Lett.*, **46**, 11,080–11,090, doi:10.1029/2019GL084961.
- Long, M. D. & Silver, P. G., 2008. The subduction zone flow field from seismic anisotropy: A global view, *Science*, **319**(5861), 315–318, doi:10.1126/science.1150809.
- Long, M. D. & Silver, P. G., 2009. Shear wave splitting anisotropy: Measurements, interpretation, and new directions, *Surv. Geophys.*, **30**, 407–461, doi:10.1007/s10712-009-9075-1.

- Luo, Y., Huang, Z.-X., Peng, Y.-J. & Zheng, Y.-J., 2004. A Study on SKS Wave Splitting Beneath the China Mainland and Adjacent Regions, *Chinese J. Geophys.* (in Chinese), **47**(5), 916–926, doi:10.1002/cjg2.569.
- Mainprice, D. & Nicolas, A., 1989. Development of shape and lattice preferred orientations: Application to the seismic anisotropy of the lower crust, *J. Struct. Geol.*, **11**(1-2), 175–189, doi:10.1016/0191-8141(89)90042-4.
- Mainprice, D. & Silver, P.G., 1993. Interpretation of SKS-waves using samples from the subcontinental lithosphere, *Phys. Earth planet. Int.*, **78**, 257–280, doi:10.1016/0031-9201(93)90160-B.
- Mardia, K.V. & Jupp, P.E., 2000, Directional statistics: New York, Wiley, 429 p.
- Ohuchi, T. & Irifune, T., 2013. Development of A-type olivine fabric in water-rich deep upper mantle, *Earth Planet. Sci. Lett.*, **362**, 20–30, doi:10.1016/j.epsl.2012.11.029.
- Pasyanos, M. E., Masters, T. G., Laske, G. & Ma, Z., 2014. LITHO1.0: An updated crust and lithospheric model of the Earth, *J. Geophys. Res.*, **119**(3), 2153–2173, doi:10.1002/2013jb010626.
- Refayee, H. A., Yang, B. B., Liu, K. H. & Gao, S. S., 2014. Mantle flow and lithosphere–asthenosphere coupling beneath the southwestern edge of the North American craton: Constraints from shear-wave splitting measurements, *Earth Planet. Sci. Lett.*, **402**, 209–220, doi:10.1016/j.epsl.2013.01.031.
- Rümpker, G. & Silver, P. G., 1998. Apparent shear-wave splitting parameters in the presence of vertically varying anisotropy, *Geophys. J. Int.*, **135**(3), 790–800, doi:10.1046/j.1365-246x.1998.00660.x.
- Savage, M. K., 1999. Seismic anisotropy and mantle deformation: What have we learned from shear wave splitting?, *Rev. Geophys.*, **37**(1), 65–106, doi:10.1029/98rg02075.
- Shan, B., Zhou, W. & Xiao, Y., 2021. Lithospheric thermal and compositional structure of South China jointly inverted from multiple geophysical observations, *Sci. China Earth Sci.*, **64**(1), 148–160, doi:10.1007/s11430-019-9661-4.
- Silver, P. G., 1996. Seismic anisotropy beneath the continents: Probing the depths of geology, *Annu. Rev. Earth Planet. Sci.*, **24**(1), 385–432, doi:10.1146/annurev.earth.24.1.385.
- Silver, P. G. & Chan, W. W., 1991. Shear wave splitting and subcontinental mantle deformation, *J. Geophys. Res.*, **96**(B10), 16429, doi:10.1029/91jb00899.

- Silver, P. G. & Savage, M. K., 1994. The Interpretation of Shear-Wave Splitting Parameters In the Presence of Two Anisotropic Layers, *Geophys. J. Int.*, **119**(3), 949–963, doi:10.1111/j.1365-246x.1994.tb04027.x.
- Van der Meer, D.G., Hinsbergen, D. J. V. & Spakman, W., 2018. Atlas of the underworld: Slab remnants in the mantle, their sinking history, and a new outlook on lower mantle viscosity, *Tectonophysics*, **723**, 309–448, doi:10.1016/j.tecto.2017.10.004.
- Vinnik, L. P., Makeyeva, L. I., Milev, A. & Usenko, A. Y., 1992. Global patterns of azimuthal anisotropy and deformations in the continental mantle, *Geophys. J. Int.*, **111**(3), 433–447, doi:10.1111/j.1365-246x.1992.tb02102.x.
- Wang, C. Y., Flesch, L. M., Chang, L. & Zheng, T., 2013. Evidence of active mantle flow beneath South China, *Geophys. Res. Lett.*, **40**(19), 5137–5141, doi:10.1002/grl.50987.
- Wessel, P., Luis, J. F., Uieda, L., Scharroo, R., Wobbe, F., Smith, W. H. F. & Tian, D., 2019. The Generic Mapping Tools version 6. *Geochemistry, Geophysics, Geosystems*, **20**, 5556–5564, doi:10.1029/2019GC008515.
- Yang, B. B., Gao, S. S., Liu, K. H., Elsheikh, A. A., Lemnifi, A. A., Refayee, H. A. & Yu, Y., 2014. Seismic anisotropy and mantle flow beneath the northern Great Plains of North America, *J. Geophys. Res.*, **119**(3), 1971–1985, doi:10.1002/2013jb010561.
- Yang, B. B., Liu, Y., Dahm, H., Liu, K. H. & Gao, S. S., 2017. Seismic azimuthal anisotropy beneath the eastern United States and its geodynamic implications, *Geophys. Res. Lett.*, **44**(6), 2670–2678, doi:10.1002/2016gl071227.
- Yang, X., Li, H., Li, Y., Lü, Q., Zhang, G., Jiang, G. & Li, X., 2019. Seismic anisotropy beneath eastern China from shear wave splitting, *Geophys. J. Int.*, **218**(3), 1642–1651, doi:10.1093/gji/ggz242.
- Zhang, S. & Karato, S.-I., 1995. Lattice preferred orientation of olivine aggregates deformed in simple shear, *Nature*, **375**(6534), 774–777, doi:10.1038/375774a0.
- Zhao, L., Zheng, T. & Lu, G., 2013. Distinct upper mantle deformation of cratons in response to subduction: Constraints from SKS wave splitting measurements in eastern China, *Gondwana Research*, **23**(1), 39–53, doi:10.1016/j.gr.2012.04.007.
- Zhao, L., Zheng, T., Chen, L. & Tang, Q., 2007. Shear wave splitting in eastern and central China: Implications for upper mantle deformation beneath continental margin, *Phys. Earth Planet. Inter.*, **162**(1-2), 73–84. doi:10.1016/j.pepi.2007.03.004.

- Zhao, L., Zheng, T., Lu, G. & Ai, Y., 2011. No direct correlation of mantle flow beneath the North China Craton to the India–Eurasia collision: constraints from new SKS wave splitting measurements, *Geophys. J. Int.*, **187**(2), 1027-1037, doi:10.1111/j.1365-246X.2011.05201.x.
- Zheng, X. F., Yao, Z. X., Liang, J. H. & Zheng, J., 2010. The role played and opportunities provided by IGP DMC of China National Seismic Network in Wenchuan earthquake disaster relief and researches, *Bull. Seismol. Soc. Am.*, **100**(5B), 2866–2872. doi:10.1785/0120090257.

II. SEISMOGENIC LAYER AZIMUTHAL ANISOTROPY IN THE VICINITY OF THE 2019 M7.1 RIDGECREST EARTHQUAKE REVEALED BY SHEAR WAVE SPLITTING ANALYSIS

ABSTRACT

To investigate the spatial and temporal variations of seismic azimuthal anisotropy in the vicinity of the July 2019 M7.1 Ridgecrest, California, earthquake, local events recorded by three seismic stations over the period of July 2019 to January 2020 were used to obtain ~800 shear wave splitting measurements. The results suggest a strong asymmetry in anisotropy forming mechanisms across the Eastern Little Lake Fault (ELLF). In the area located to the northeast of the ELLF, the observed fast orientations are dominantly N-S, which is parallel to the maximum horizontal compressive stress, and the splitting times are independent of the focal depths, suggesting that stress induced anisotropy is mostly located in a shallow layer in the top ~5 km. In the area southwest of the ELLF, the fast orientations are mostly parallel to the strike of fault zones. Such parallelism is most clearly observed in the section of the ELLF between the main section of the Southern Little Lake Fault (SLLF) and the North SLLF, where the halfwidth of the fault zone estimated based on the splitting measurements is at least 3.5 km and is consistent with the diffusive distribution of earthquakes. NE-SW oriented anisotropy in the vicinity of a proposed blind fault confirms the existence of the fault. A nearly 90-degree switch in the fast orientations and greatly reduced splitting times from a group of nearby earthquakes may indicate fault zone healing.

1. INTRODUCTION

The July 2019 Ridgecrest, California earthquake sequence, consisting primarily of an M6.4 foreshock, an M7.1 mainshock, and tens of thousands of recorded aftershocks, activated a complex network of intertwined conjugate faults in the southern Walker Lane (Figure 1) (e.g., Barnhart et al., 2019; DuRoss et al., 2020; Fielding et al., 2020; Hauksson et al., 2020; C. Liu et al., 2019; Ponti et al., 2020; Ross et al., 2019; Shelly, 2020). The activated fault network mainly includes the NW-SE striking Eastern Little Lake Fault (ELLF) and the NE-SW striking Southern Little Lake Fault (SLLF) and several other faults (Figure 1b) (Hauksson et al., 2020; Plesch et al., 2020). In addition to the surface ruptures, Shelly (2020) and Plesch et al. (2020) reported several possible NE-SW blind faults that are approximately normal to the ELLF. The averaged maximum horizontal compressive stress (SHmax) direction obtained from focal mechanism inversions in the Ridgecrest area is nearly N-S, and a rotation of a few degrees after the mainshock has been proposed (Figure 1b; Duan et al., 2022; Hardebeck, 2020; Sheng & Meng, 2020; Wang & Zhan, 2020).

Although many studies have been conducted after the 2019 Ridgecrest earthquake sequence to understand surface deformation and stress field distribution and evolution (e.g., Chen et al., 2020; DuRoss et al., 2020; Fielding et al., 2020; Ross et al., 2019; Shelly, 2020; Sheng & Meng, 2020), one important type of measurements that is still missing is the spatial and possible temporal variations of azimuthal anisotropy in the seismogenic zone. While GPS and remote sensing-based techniques map the deformation field at the surface and focal mechanism solutions provide insights into the stress regime

in the fault zones, seismic anisotropy measurements, like those presented below, have the potential to provide critical information about the deformation field in the seismogenic zone (e.g., Boness & Zoback, 2004; Cochran et al, 2003; Crampin, 1987; T. Li et al., 2019; Z. Li et al., 2014; Y. Liu et al., 2021; Shi et al., 2020).

1.1. SHEAR WAVE SPLITTING ANALYSIS AND SEISMOGENIC LAYER AZIMUTHAL ANISOTROPY

Shear wave splitting (SWS) analysis is one of the most frequently employed techniques to map azimuthal anisotropy along the ray paths (Crampin, 1991, 1994; Jiang et al., 2021; Y. Liu et al., 2008; Miller & Savage, 2001; Peng & Ben-Zion, 2004). The linearly polarized shear wave splits into two nearly perpendicular quasi-shear waves with different speeds when it propagates through an anisotropic medium (Ando, 1980; Silver & Chan, 1991). The polarization orientation of the fast wave (fast orientation or ϕ) and the time of separation between the fast and slow waves (splitting time or δt) are unambiguous indicators of the orientation and strength of azimuthal anisotropy, respectively.

Azimuthal anisotropy developed in the brittle upper continental crust is typically attributed to localized tectonic stress-controlled fluid-filled microcracks and is mostly parallel to the SHmax direction. Anisotropy such formed is termed stress-induced anisotropy (Boness & Zoback, 2004; **Crampin**, 1978, **1987**, **1993**; Leary et al., 1990). Anisotropy can also be associated with rock or mineral structures (Boness & Zoback, 2006) with an orientation that is consistent with the dominant strike of fracture zones such as those associated with active faults, i.e., structure-induced anisotropy (Z. Li & Peng, 2017; Zhang & Schwart, 1994; Zinke & Zoback, 2000). Moreover, other

mechanisms such as magmatic dikes and oriented melt pockets (Bastow et al., 2010; S. Gao et al., 1997; Holtzman et al., 2003; Keir et al., 2005), preferential mineral alignment (Brocher & Christensen, 1990; Okaya et al., 2016; Sayers, 1994) and sedimentary layering (Alford, 1986; Audet, 2015; Bastow et al., 2010; Leary et al., 1990) can also cause crustal anisotropy.

1.2. RATIONALE OF THE STUDY

Most previous SWS studies of seismogenic zone anisotropy use station-averaged or area-averaged splitting parameters (e.g., Kaneshima, 1990; Z. Li & Peng, 2017; Y. Liu et al., 2008; Wu et al., 2019), which are not ideal for revealing ray-path specific anisotropic variations that are observable in areas with complex structures and heterogeneous stress fields. In this study, we utilize individual rather than station- or area-averaged measurements to identify spatially varying anisotropy in the seismogenic layer in the vicinity of the southern Ridgecrest aftershock zone (Figure 1a). In addition to spatial variations, we also attempt to explore possible temporal variations of anisotropy in the seismogenic zone, which may reflect rock property changes as a result of fluid injection (e.g., T. Li et al., 2019; Miller & Savage, 2001; Volti & Crampin, 2003), perturbation of the local stress field (e.g., Y. Gao & Crampin, 2003, 2004; Hiramatsu et al., 2010), changes in rock and static stress physical properties related to large earthquakes (e.g., Crampin, 1994; Crampin et al., 1990; Y. Gao et al., 1998; Y. Liu et al., 1997; Lucente et al., 2010), and fault zone healing processes after a major earthquake (e.g., Hiramatsu et al., 2005; Tadokoro & Ando, 2002). Seismic events from almost identical ray paths are employed in this study to remove spatial effects (e.g., Aster et al.,

1990; Bokelmann & Harjes, 2000; Y. Liu et al., 2004; Peng & Ben-Zion, 2004) to explore possible fault healing following the M7.1 Ridgecrest earthquake.

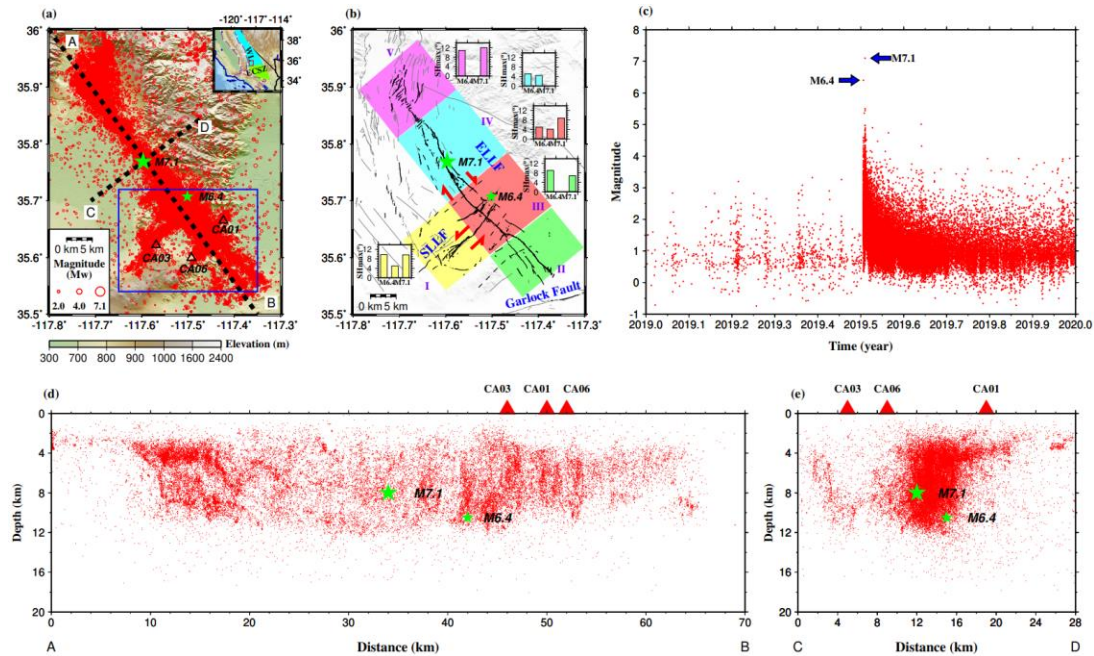


Figure 1. (a) Distribution of seismic stations used in the study (black triangles) and earthquakes that occurred in 2019 (red dots). The green stars show the epicenters of the M6.4 (4 July 2019), and M7.1 (6 July 2019) earthquakes. The study area is marked by a blue rectangle. The inset map in the upper-right corner shows the location of the main map. WL: Walker Lane; ECSZ: Eastern California Shear Zone. (b) Fault network in the 2019 Ridgecrest aftershock zone. The grey, black solid, and black dashed lines indicate the Quaternary faults (Wills, 1988), and the surface ruptures (DuRoss et al., 2020; Ponti et al., 2020) and the blind faults (Hauksson et al., 2020; Plesch et al., 2020) formed after the M7.1 Ridgecrest earthquake sequence, respectively. The colored polygons and histograms show the distribution and variations of the orientation of the maximum horizontal compressive stress (SHmax) in different subzones (I-V) of the mapped area (Sheng & Meng, 2020). In each of the histograms, the columns from left to right represent the SHmax in the time-period prior to the M6.4 foreshock, between the M6.4 and M7.1 earthquakes, and after the M7.1 mainshock, respectively. (c) A plot of earthquake magnitudes against origin times. (d) Distribution of earthquakes projected to Profile A-B in (a). (e) Distribution of earthquakes projected to Profile C-D in (a).

2. DATA AND METHODS

The seismic dataset used in this study was recorded by three temporary stations (CA01, CA03, and CA06) located in the southern aftershock zone of the 2019 Ridgecrest earthquake sequence and was obtained from the Incorporated Research Institutions for Seismology (IRIS) Data Management Center (DMC) (Figure 1a). The stations were deployed by the U.S. Geological Survey (USGS; Cochran et al., 2020) following the M6.4 foreshock and M7.1 mainshock. These stations collected data with a recording length of about 4–6 months until January 2020. A total of 60,367 earthquakes were reported in the mapped area of Figure 1a during 2019 and were relocated by the Southern California Earthquake Data Center (<https://scedc.caltech.edu/>; Figure 1). For data requests, we apply a minimum cutoff magnitude of -0.74, which is the minimum magnitude in the catalog, to ensure that all recorded seismic events can be accessed and processed. To avoid the distortion of particle motions of the direct S-wave by the free surface, only events with an angle of incidence of less than 40° (e.g., Booth & Crampin, 1985; Nuttli, 1961) are used for SWS analysis in this study.

Using a semi-automatic procedure (K.H. Liu et al., 2008; K.H. Liu & S.S. Gao, 2013) developed based on the principle of minimizing the lesser of two eigenvalues of the covariance matrix (Silver & Chan, 1991), we simultaneously search for the initial polarization direction and the optimal pairs of splitting parameters (including the fast orientation and splitting time). Once the initial polarization direction and the splitting parameters are found, the horizontal seismograms are rotated to the radial and transverse components (which are relative to the direction of the initial polarization direction and

not the great circle arc). The corrected radial and transverse components, the fast and slow components, the particle motion patterns, and the remaining energy on the corrected transverse components are then computed, in the same manner as the minimization of transverse energy approach (Silver & Chan, 1991), for visual display and manual checking. The original seismograms are initially bandpass filtered with corner frequencies of 0.5 and 10.0 Hz. All the resulting measurements are automatically ranked and subsequently visually verified. If necessary, the beginning and end of the window for SWS analysis and the band-pass filtering frequencies are modified during the manual checking stage to exclude non-S arrivals and improve the signal-to-noise ratio. The final ranking of the measurements is determined based on the quality of the signal, the linearity of the corrected particle motions, and the uniqueness and strength of the minimum energy point on the misfit map of the corrected transverse component. Examples of splitting analysis from the three stations used in the study are shown in Figure 2.

3. RESULTS

After manual checking, a total of 803 pairs of well-defined optimal splitting parameters are obtained, among which 253 are from Station CA01, 230 from Station CA03, and 320 from Station CA06. Table A1 shows station-averaged splitting parameters. The measurements are from 796 events with magnitudes ranging from 0.1 to 3.8. For all the measurements, the circular mean of the fast orientations is $9.8 \pm 24.2^\circ$, the arithmetic mean of the delay times is 0.05 ± 0.03 s, and the mean ray-path-length normalized

splitting time (NST) is 5.99 ± 3.11 ms/km. Measurements from each of the three stations can be found in Figures 3–5, where the splitting parameters are plotted at the epicenter. Figure A1 shows results plotted at the middle points between the events and the stations.

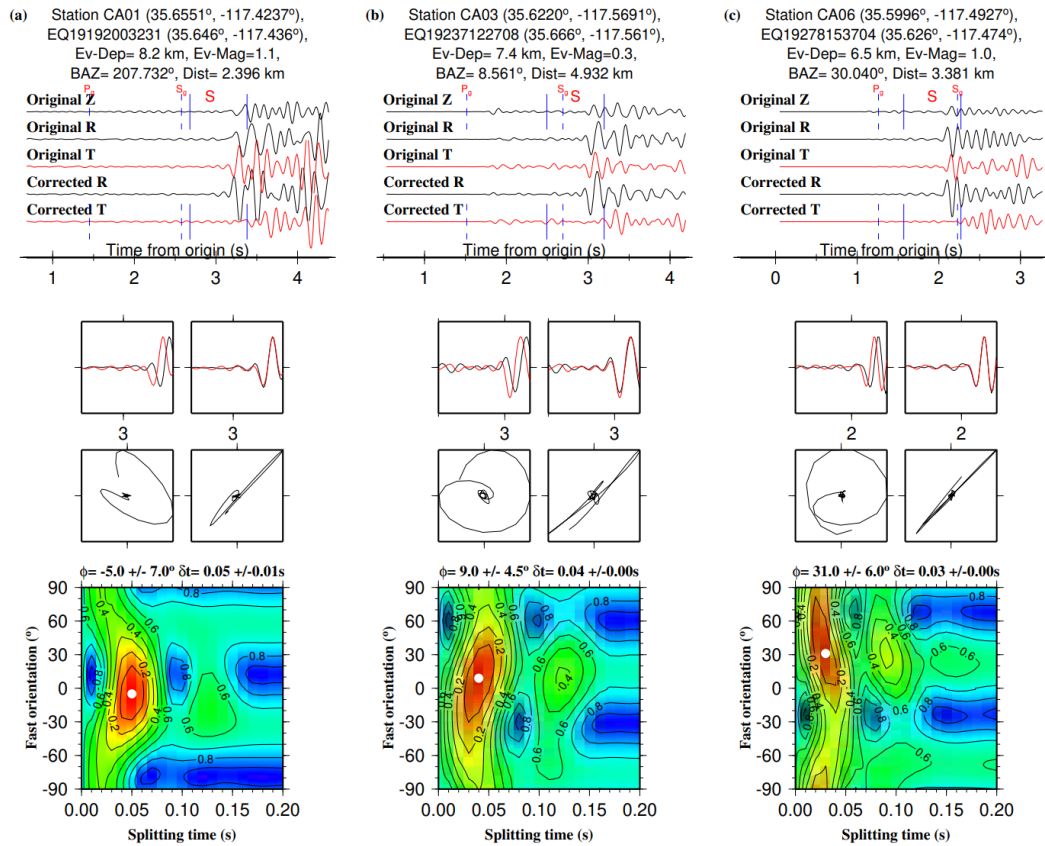


Figure 2. Examples of SWS measurements from Stations CA01, CA03, and CA06. For each column, the plots in the top row show the original vertical component and original and corrected radial and transverse components, and the plots in the central rows show the uncorrected and corrected particle motions of the fast and slow particles. The bottom plots are corrected transverse energy contour maps, with the color representing the energy on the corrected transverse component. The optimal pair of splitting parameters correspond to the minimum value on the contour map of the remaining transverse component energy and are indicated by a white dot.

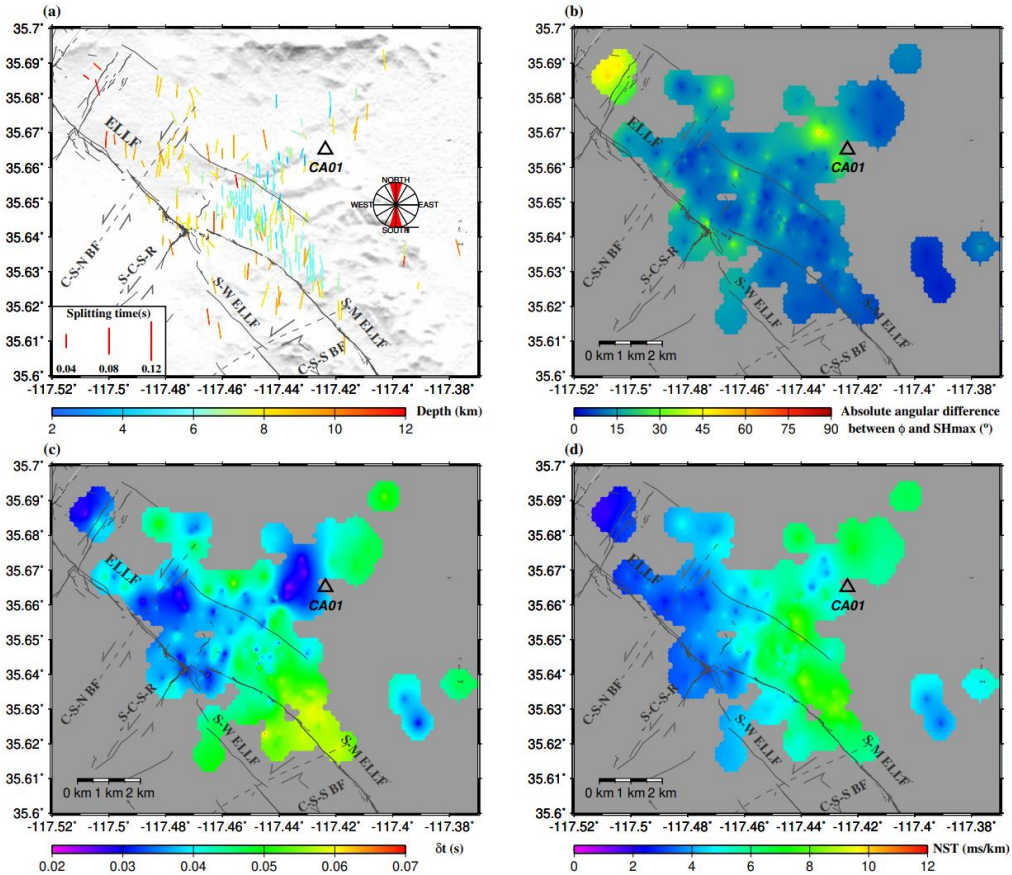


Figure 3. (a) Resulting SWS parameters of Station CA01 plotted at the epicenters. The orientation of the bars represents the fast orientation, and the length is proportional to the splitting time. The color of the bars indicates focal depths, and the rose diagram is created using all the fast orientation measurements from this station. (b) Absolute angular difference between fast orientations and SHmax direction (Sheng & Meng, 2020). (c) Splitting time measurements. (d) Ray path normalized splitting times. S-M ELLF: South-Main branch of the ELLF; S-W ELLF: South-West branch of the ELLF; C-S-N BF: Cross-South-North blind fault; C-S-S BF: Cross-South-South blind fault. S-C-S-R: Short-Cross-Sinistral-Rupture.

3.1. STATION CA01

Station CA01 is the only station used in this study that is located to the northeast of the ELLF (Figure 1). Figure A2 shows 4 typical measurements from this station. The majority of the events used to obtain the splitting measurements from this station are also

distributed to the northeast of the ELLF and thus, only a few ray paths travel through the ELLF, which is the most significant fault in the study area (Figure 3). The resulting fast orientations are dominantly N-S and correlate with the SHmax orientation (Figures 3a and 3b). The splitting times from events near the South-Main and South-West branches of the ELLF are slightly (about 0.01–0.03 s) larger than those in other areas (Figure 3c). Seismic events in the north of the South-Main branch of the ELLF have relatively shallower foci, while the corresponding NSTs are greater (Figures 3a and 3d). Despite the complicated fault structures around Station CA01, there are no systematic spatial variations in both the fast orientations and splitting times observed at this station.

3.2. STATION CA03

Station CA03 is situated inside the fault zone of the southwest part of the SLLF (Figure 4). The measurements show considerable and spatially systematic variations (see Figure A3 for examples) and can be divided into four groups depending on the characteristics of the observed splitting parameters (Figure 4a).

Group 1 contains measurements located approximately 5 km north of the station, near the southwest end of the north branch of the SLLF (North SLLF). This group of measurements show SHmax-parallel (N-S) fast orientations with small splitting times (~ 0.03 s) and NSTs (~ 3 ms/km). In addition, splitting parameters from events located to the north of the faults are indistinguishable with those from events to the south of the fault (Figure 4).

Group 2 includes measurements from events located ~ 8 km northeast of the station, close to the interlocked conjugate fault zone that comprises the right-lateral

ELLF, the left-lateral SLLF, and the left-lateral North SLLF. Measurements in this group mostly display NW-SE fast orientations that align well with the trend of the ELLF. The fast orientations for events in this group are mostly NW-SE, and become E-W for events in the southern part of the area (Figure 4a). The splitting times and NSTs in this group are the largest in the study area (Figures 4c and 4d).

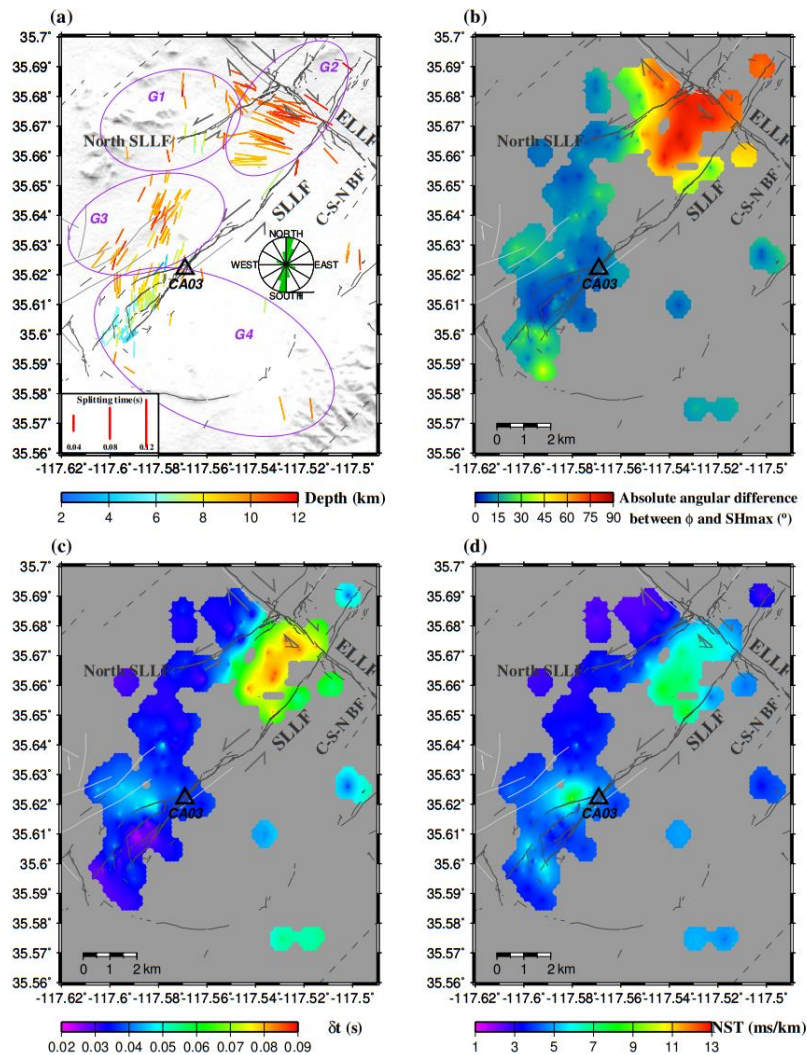


Figure 4. Same as Figure 3 but for Station CA03. North SLLF: north branch of the SLLF.

Group 3 measurements are from events located within ~3 km from the station in the northwest quadrant. Most of these measurements are distributed along the Quaternary faults that run sub-parallel to the SLLF and exhibit NE-SW fast orientations (Figures 4a and 4b). In general, events closer to Station CA03 have shallower focal depths (mostly shallower than 8 km), while the depths of those closer to the Quaternary faults are deeper than 8 km (Figure 4a). Except for the measurements observed from events near the station, the resulting splitting times and NSTs are relatively small (Figures 4c and 4d).

Events in Group 4 are mainly from the southwest branches of the SLLF. The resulting fast orientations of these measurements are mostly parallel to the N-S oriented SHmax direction, and a few measurements from events located at the southwest end of the SLLF demonstrate SLLF-parallel fast orientations (Figures 4a and 4b). Events in the southwest branches of the SLLF are mainly concentrated at shallower depths with smaller splitting times than events in the rest of Group 4 (Figures 4a and 4c).

3.3. STATION CA06

Measurements from Station CA06 are mainly from events located in the area between the ELLF and the SLLF (Figure 5). The fast orientations from events located southwest of the ELLF dominantly agree with the strike of the Cross-South-South and Cross-South-North blind faults and other NE-SW oriented cross faults. In contrast, for measurements from events in the off-fault areas or along the ELLF, the fast orientations deflect towards the SHmax direction (Figures 5a and 5b). The splitting times observed at this station range from 0.02 to 0.12 s with a mean value of 0.07 ± 0.03 s, and the NSTs

range from 1.45 to 20.35 ms/km with a mean value of 7.53 ± 3.85 ms/km. Events whose ray paths travel through the fault zone between the Short-Cross-Sinistral-Rupture (DuRoss et al., 2020) and the Cross-South-South blind fault (Hauksson et al., 2020; Plesch et al., 2020) have significantly greater δt and NST values (Figures 5c and 5d). Some of the measurements have two possible pairs of splitting parameters (e.g., Figures A5 and A6) and might be related to cycle skipping, as discussed below.

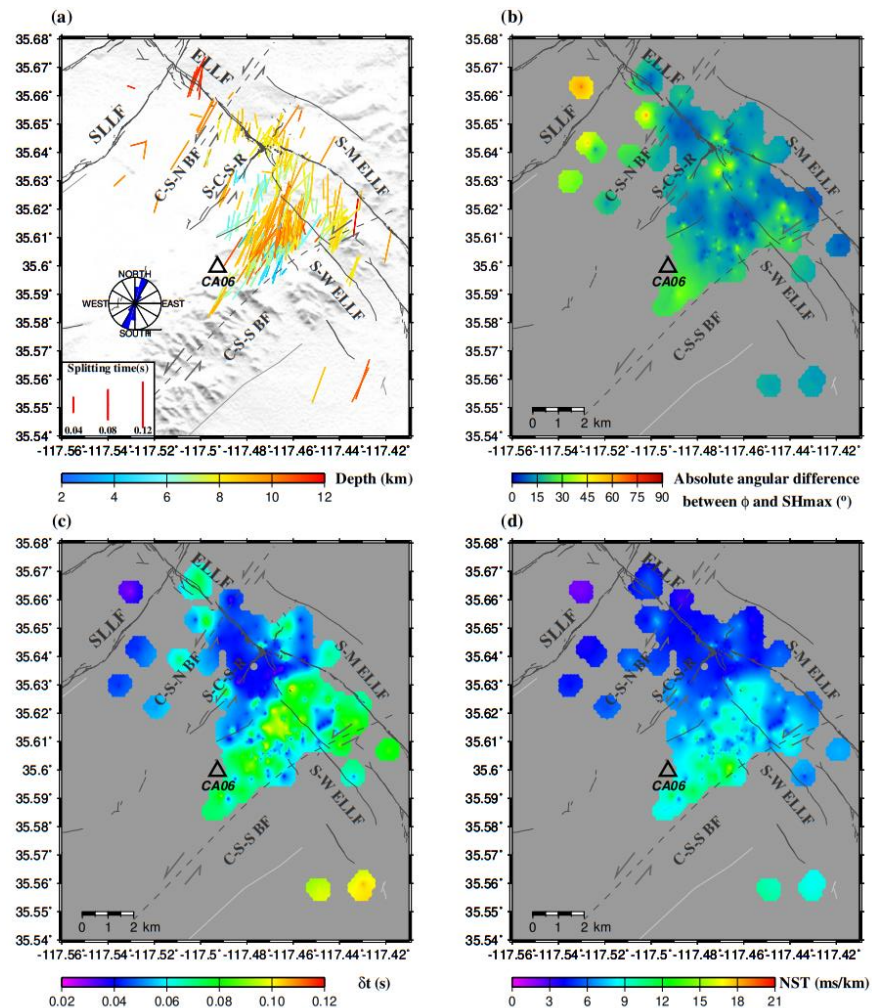


Figure 5. Same as Figure 3 but for Station CA06.

4. DISCUSSION

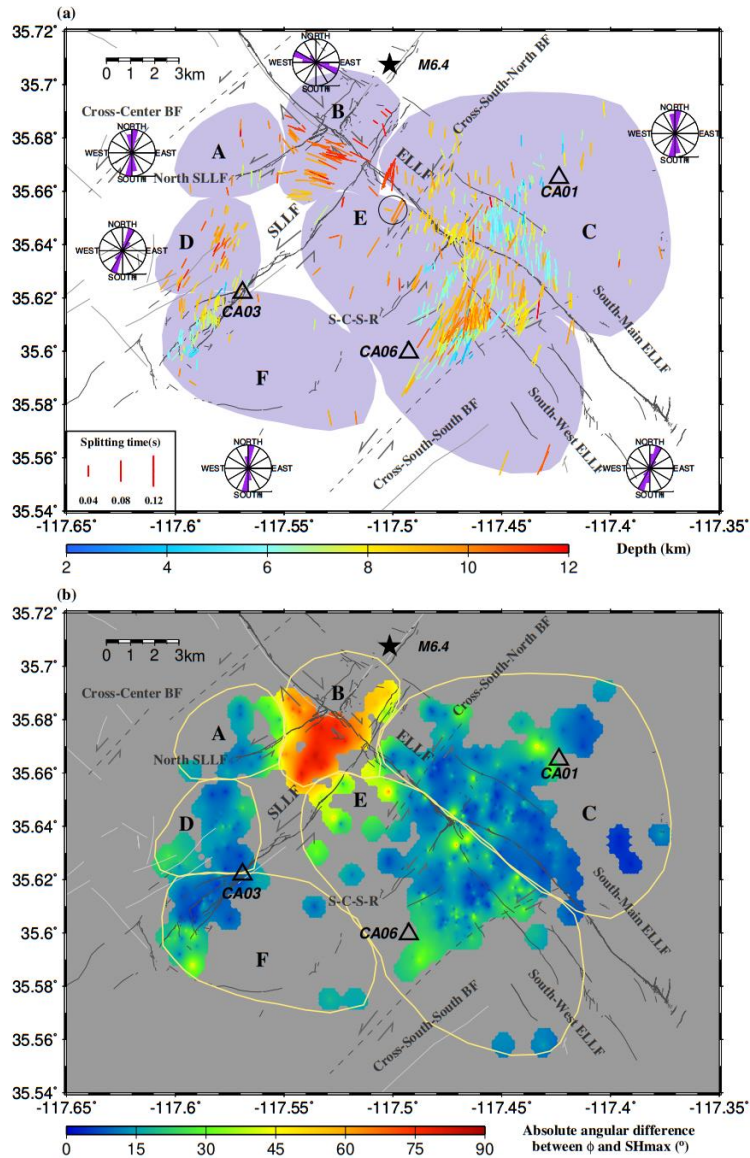


Figure 6. (a) Same as Figure 3a but for SWS parameters observed by all three stations. The shaded areas are subdivisions of the whole study area. Measurements in the black circle near the center of the diagram show temporal variations. (b) Same as Figure 3b but for all the measurements from the three stations.

To facilitate discussion, in the following we divide the study region into six areas (Areas A–F; Figure 6) based on the main characteristics of the splitting parameters.

Areas A, D, and F contain the measurements from Groups 1, 3, and 4 of Station CA03, respectively. Area B includes measurements from Group 2 of Station CA03 and a few from Stations CA01 and CA06. Area C includes the area northeast of the ELLF and southeast of the SLLF, and the measurements are mostly from Station CA01 plus a few from CA06. Area E contains all the measurements located southwest of the ELLF and southeast of the SLLF, mainly from Station CA06 and, to a lesser extent, from Stations CA01 and CA03. Figures 6 and 7 show the measurements plotted at the epicenters, and in Figure A1, they are displayed at the middle points between the stations and the epicenters. The average measurements for each of the areas can be found in Table A2.

Note that when the measurements are interpreted, it is important to realize that the observed anisotropy is accumulated along the entire ray path in spite of the fact that they are displayed at the epicenters in Figures 6 and 7 or at the middle points between the epicenters and stations in Figure A1. Additionally, the ray path samples a “banana” shaped Fresnel zone with a size that is dependent on the frequencies and distance to the station. For instance, the radius of the first Fresnel zone for a 7 Hz S-wave is about 1 km at a distance of 5 km from the station.

4.1. CYCLE SKIPPING

Some previous studies of upper crustal anisotropy using splitting of local S-waves have identified that the SWS results may suffer from cycle skipping that mostly arises from the sinusoidal nature of seismic waveforms (e.g., Gerst, 2003; Johnson et al., 2010; Matcham et al., 2000; Peng & Ben-Zion, 2004; Savage et al., 2010, 2015). For instance, cycle skipping can occur when the first trough of the slow wave coincides with the first

peak of the fast wave, or when the slow wave lags the fast wave by more than one cycle. Cycle skipping typically results in a splitting time error of multiples of half of the dominant period or a fast orientation error of 90° (Walsh, 2012).

Some of the events recorded by Station CA06 have two pairs of possible optimal measurements, as reflected by the presence of two regions of comparable low values on the corrected transverse energy contour map (e.g., the bottom panel of Figures A5a and A6a). The separation of the two possible splitting times (~ 0.07 s) is approximately half of the dominant period of the S-wave (~ 0.15 s), which is indicative of cycle skipping, and the two fast orientations are similar to each other. To decide the most likely optimal splitting parameter pair, we visually check all the measurements with two possible sets of measurements (e.g., Figures A5a and A6a), and adjust the S-wave time window so that one of the two possible splitting parameter pairs has the lowest remaining energy on the corrected transverse component. We then re-adjust the S-wave window so that the other parameter pair has the minimum energy (Figures A5 and A6). The optimal pair is selected by comparing the two sets of measurements based on the following two criteria: 1) The time window leading to the minimum transverse energy contains at least one cycle of S-wave; and 2) the resulting fast and slow components have a better match than the other pair (and thus the particle motion pattern is more linear). The resulting splitting parameters determined using the above procedure are spatially consistent (Figure 5), suggesting that the optimal measurements are correctly selected at the vast majority of the station-event pairs with the possible presence of cycle skipping.

orientation of SHmax can be clearly observed in Figure 6b. The match between the two orientations is reduced for measurements from events in the southwestern terminus area of the SLLF in Area F and may reflect the influence of fault zone anisotropy. Interestingly, a better match is observed for measurements from events in the fault zone immediately to the southwest of Station CA03 (Figure 6b). A possible explanation for this difference is that relative to the latter group of events, events in the former group are shallower (Figure 6a) and more distant from the station (CA03), and thus the ray paths from the events to the station sample a greater portion of the fault zone.

Although the focal depths vary considerably in the three areas (Figure 6a), the splitting times are largely independent of the focal depths (Figure 7a), suggesting that regional stress induced anisotropy is concentrated at shallow depths, probably above ~5 km, which is the focal depths for most of the shallowest events. The largest splitting times in the three areas are observed from events in the southwestern part of Area C adjacent to the South-Main ELLF (Figure 7a). A possible cause of the large splitting times in this area is reduced rock strength associated with the intensive deformation in the fault zone, leading to more developed SHmax-parallel micro-fractures.

4.3. ANISOTROPY ASSOCIATED WITH SURFACE AND BLIND FAULTS (AREAS B, D, AND E)

The fast orientations from events in Areas B, D, and E are significantly different from the SHmax orientation but are largely parallel to the surface expression of known faults or the strike of previously proposed blind faults, suggesting fractures in the fault zones are mostly responsible for the observed anisotropy. The observed fast orientations

and splitting times provide constraints on the lateral and depth extents of the fault zones, as detailed below.

The section of the ELLF in Area B demonstrates the clearest parallelism between the fast orientations and the fault strike (Figure 6a), and the section between the SLLF and the North SLLF hosts some of the largest splitting times in the entire study area (Figure 7a), where fault parallel fast orientations are still observable (by Station CA03) for events located ~2 km away from the surface expression of the fault. Assuming an anisotropy magnitude of 5%, a 0.06 s splitting time for an event with a focal depth of 10 km and an epicentral distance of 6 km approximately requires a horizontal dimension of 1.5 km for the fault-parallel zone of anisotropy, suggesting that the half-width of the ELLF in Area B between the SLLF and the North SLLF is at least 3.5 km. This wide fault zone is consistent with the diffusively distributed earthquakes in the block border by the SLLF and the North SLLF (Figure A7). In contrast, no ELLF-parallel anisotropy is observed in the section of the ELLF south of the SLLF, an observation that is consistent with the sharp reduction in the apparent width of the fault zone across the SLLF (Figure A7).

The NE-SW fast orientations from events in Area D indicate the presence of well developed along strike fractures associated with the SLLF and minor faults in the area. Relative to the section of the ELLF north of the SLLF, fractures associated with the North SLLF are significantly less developed, as indicated by the lack of fault parallel anisotropy. In Area E, strong NE-SW oriented anisotropy is observed by Station CA06 for events in the vicinity of two proposed NE-SW blind faults (the Cross-South-South

and Cross-South-North blind faults), which is consistent with the area of significant velocity contrast across the blind faults reported by White et al. (2021).

4.4. ASYMMETRY IN ROCK STRENGTH ACROSS THE ELLF

One of the most intriguing features in the observed seismogenic zone anisotropy pattern is that the ELLF serves as a boundary between two regions of fast orientations. The area northeast of the fault is dominated by N-S fast orientations that are most likely formed by regional compressional stress, and fast orientations observed in the area to the southwest of the fault are generally fault parallel (Figure 6a). Such a contrast suggests that the seismogenic zone of the former area is less fractured by the strike-slip fault system, probably due to an asymmetry in the strength of the upper crust. This is consistent with the observation that most of the NE-SW oriented faults are located in the area to the southwest of the ELLF or extend a short distance across it.

4.5. POSSIBLE TEMPORAL VARIATIONS OF THE OBSERVED ANISOTROPY

Temporal variations in the strength and orientation of upper crustal anisotropy may reflect regional stress changes or significant tectonic movements related to coseismic or postseismic processes (e.g., Crampin, 1994; Y. Gao & Crampin, 2003, 2004; Y. Liu et al., 1997; Tadokoro & Ando, 2002). For instance, a set of 7 measurements at Station CA06 from seismic events located in the intersection area of the ELLF and the cross-south-north blind fault (the black circle in Figure 6a) exhibits clear temporal variations in both the fast orientation and splitting time (Figure 8). As shown in Figures 6 and A8, for the four events that occurred between days 215 and 233 in 2019,

the fast orientations are orthogonal to the ELLF and the splitting times are 0.09–0.10 s, which are among the largest in the study area (Figures 8a–8d). In contrast, the fast orientations from the three events between days 299–329 changed to parallel to the strike of the ELLF, and the splitting times reduced to 0.03 s (Figures 8e–8g). The observed splitting parameters in the same group are almost identical to each other. Note that this high level of similarity, together with the fact that the foci of the events are less than 1 km (~0.75 km) from each other, resulted in an apparently reduced number of measurements (from 7 to 3) in Figure 6a.

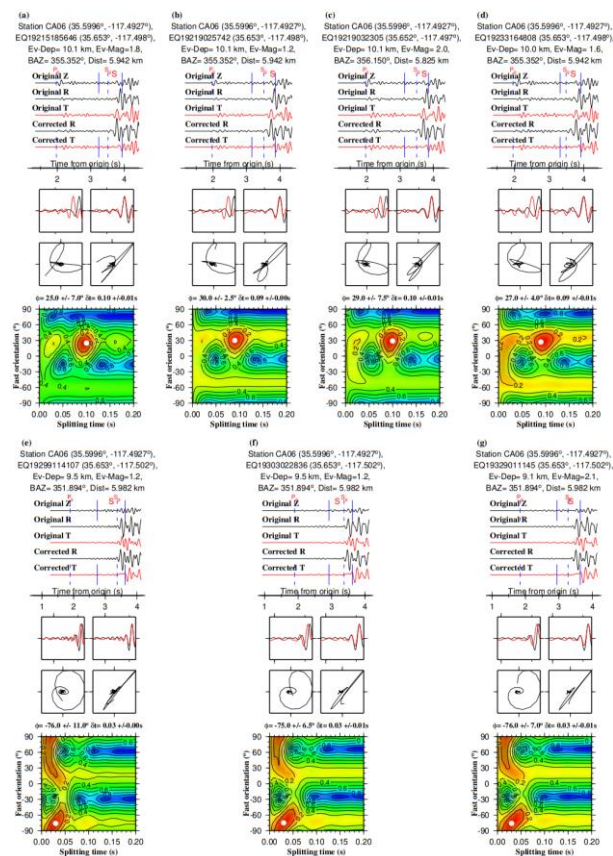


Figure 8. Measurements from 7 events in the black circle in Figure 6a that show apparent temporal variations.

The ray paths of the seven measurements traverse a group of NE-SW oriented conjugate faults and perhaps also the NW-SE oriented shear zone of the ELLF (Figure 6a). Therefore, the NE-SW fast orientations observed in the earlier group of events may indicate the existence of fractures associated with the conjugate fault system that were developed or reactivated by the M7.1 earthquake. The fact that the fast orientations changed to ELLF parallel in the later group may suggest healing of the conjugate faults, as observed elsewhere (e.g., Hiramatsu et al., 2005; Tadokoro & Ando, 2002), and anisotropy associated with the ELLF became dominant along this particular ray path.

5. CONCLUSIONS

Based on 803 pairs of splitting parameters observed by three stations in the southern 2019 Ridgecrest aftershock zone, systematic spatial variations in seismogenic zone azimuthal anisotropy are revealed. Anisotropy in the area to the northeast of the ELLF is mostly N-S oriented and is the result of regional compressive stress, and that to the southwest of the ELLF is dominated by shear zones associated with two groups of active faults. The different anisotropy forming mechanisms imply an asymmetry of rock strength across the ELLF. Significant variations in the width of the damaged zone along the ELLF are observed. The northern section of the ELLF in the study area demonstrates the strongest fault-parallel anisotropy, followed by the SLLF and the Cross-South-South and Cross-South-North blind faults. Fault-parallel anisotropy is not observed by events with ray paths traversing the North SLLF and the central and southern segments of the ELLF, which may indicate narrower and less developed fault zones relative to the

northern part of the ELLF. A clear temporal variation of anisotropy is observed near the intersection between the ELLF and the Cross-South-North blind fault and may indicate healing of NE-SW oriented faults.

ACKNOWLEDGMENTS

The facilities of IRIS Data Services, and specifically the IRIS Data Management Center, were used for access to waveforms and related metadata used in this study. IRIS Data Services are funded through the Seismological Facilities for the Advancement of Geoscience (SAGE) Award of the National Science Foundation under Cooperative Support Agreement EAR-1851048. This study was partially supported by the U.S. National Science Foundation under awards 1830644 to K. L. and S. G. and 1919789 to S.G.

DATA AVAILABILITY STATEMENT

All the Local seismic data used in this study are publicly available from the IRIS Data Management Center (<https://ds.iris.edu/ds/nodes/dmc>; Last accessed: January 2020), and the catalog of the relocated hypocenters was obtained from the California Earthquake Data Center (<https://scedc.caltech.edu/>).

APPENDIX

Table A1. Station-averaged splitting parameter results.

	φ ($^{\circ}$)	δt (s)	NST (ms/km)	Number
CA01	179.3 ± 14.7	0.04 ± 0.01	5.41 ± 1.96	253
CA03	7.1 ± 36.1	0.04 ± 0.02	4.50 ± 1.72	230
CA06	19.5 ± 17.2	0.07 ± 0.03	7.53 ± 3.85	320
All	9.8 ± 24.2	0.05 ± 0.03	5.99 ± 3.11	803

Table A2. Area-averaged splitting parameter results.

	φ ($^{\circ}$)	δt (s)	NST (ms/km)	Number
Area A	179.3 ± 6.8	0.03 ± 0.01	3.19 ± 0.83	16
Area B	113.4 ± 17.7	0.06 ± 0.02	5.27 ± 2.14	61
Area C	1.8 ± 13.8	0.05 ± 0.02	5.55 ± 2.01	285
Area D	23.9 ± 9.1	0.04 ± 0.01	4.08 ± 1.65	57
Area E	20.0 ± 18.2	0.06 ± 0.03	7.64 ± 3.98	290
Area F	6.2 ± 16.4	0.03 ± 0.01	7.64 ± 3.98	94

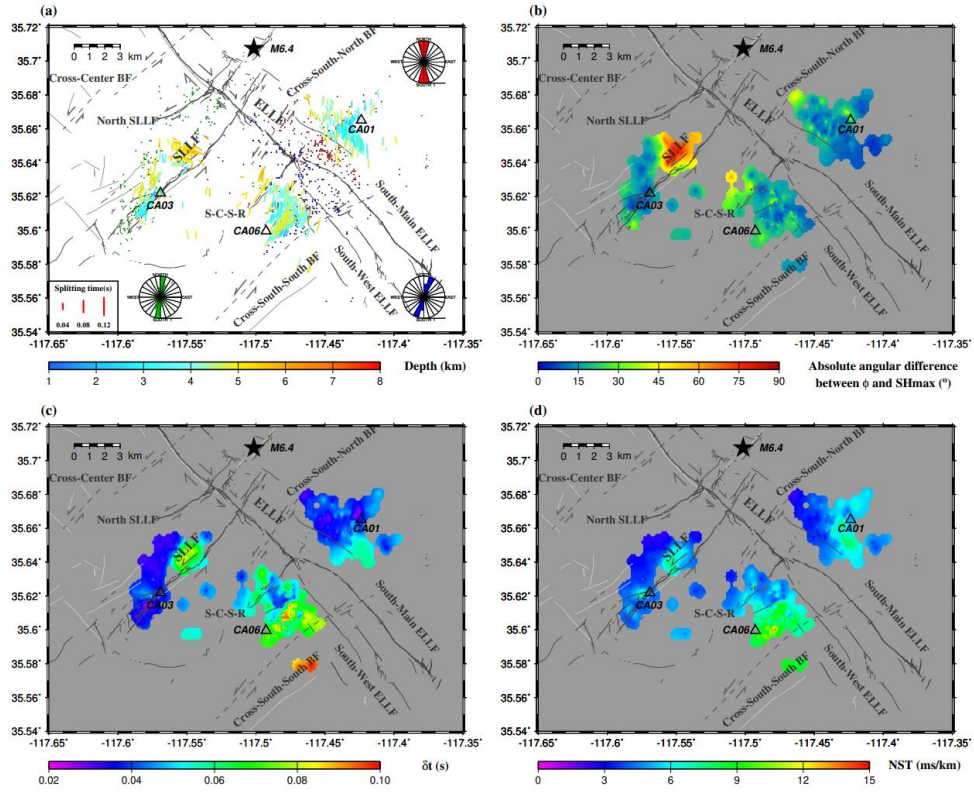


Figure A1. Same as Figures 6 and 7 in the main text but the measurements are displayed at the middle points between the epicenters and stations.

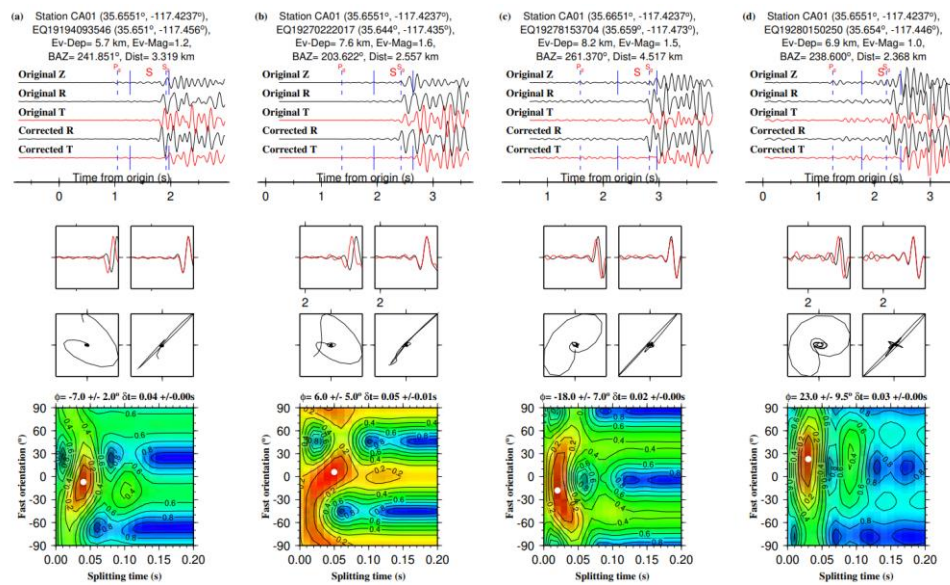


Figure A2. Examples of shear wave splitting measurements from Station CA01. See Figure 2 in the main text for details.

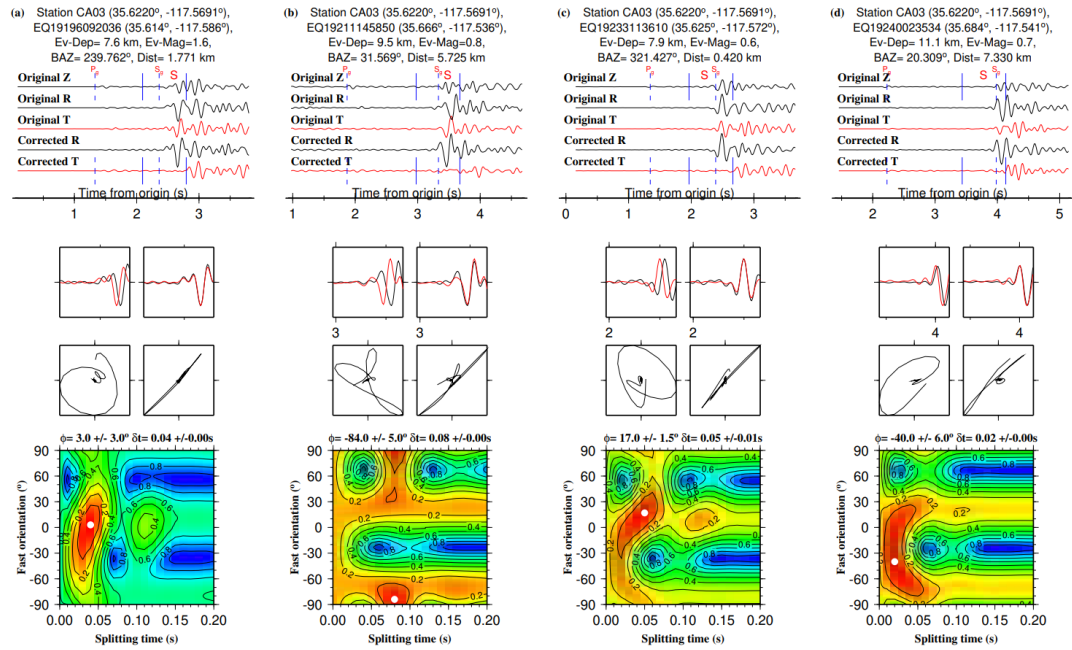


Figure A3. Same as Figure A2 but for Station CA03.

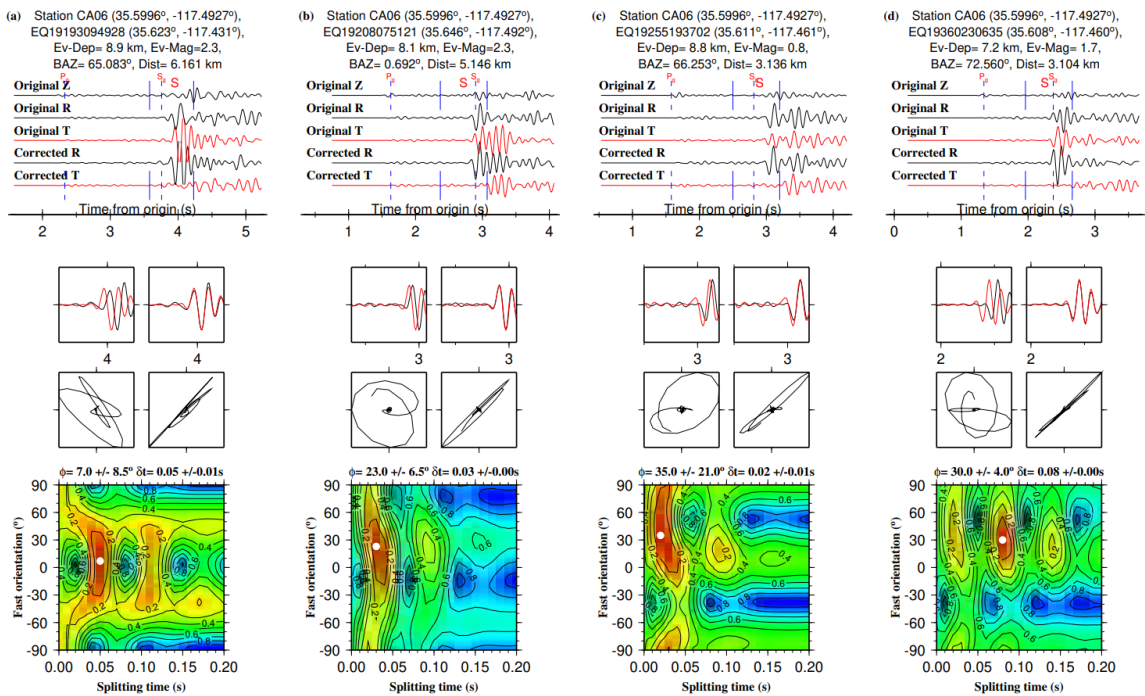


Figure A4. Same as Figure A2 but for Station CA06.

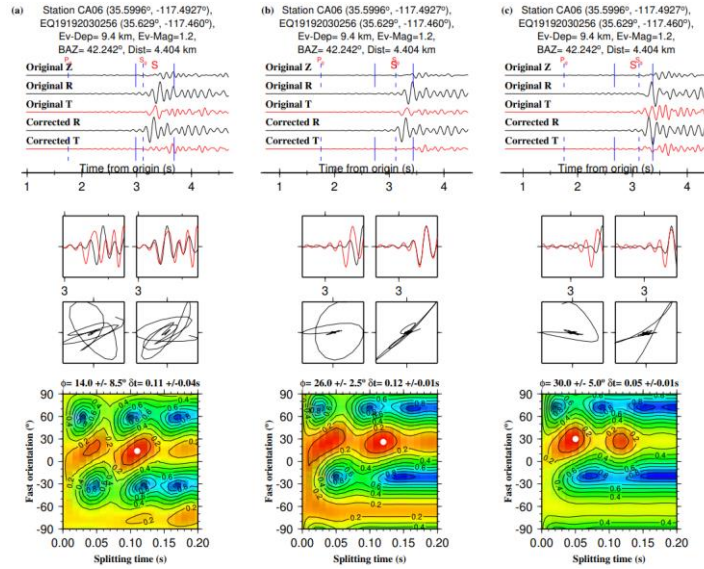


Figure A5. An event recorded by Station CA06 to demonstrate the effects of cycle skipping. (a) Results using a long S-wave section. (b) Results after adjusting the beginning and end times to reach an optimal match between the fast and slow components. (c) Results from another time window that includes only the first half cycle of the S-wave, leading to a reduced match between the fast and slow components relative to the optimal situation shown in (b).

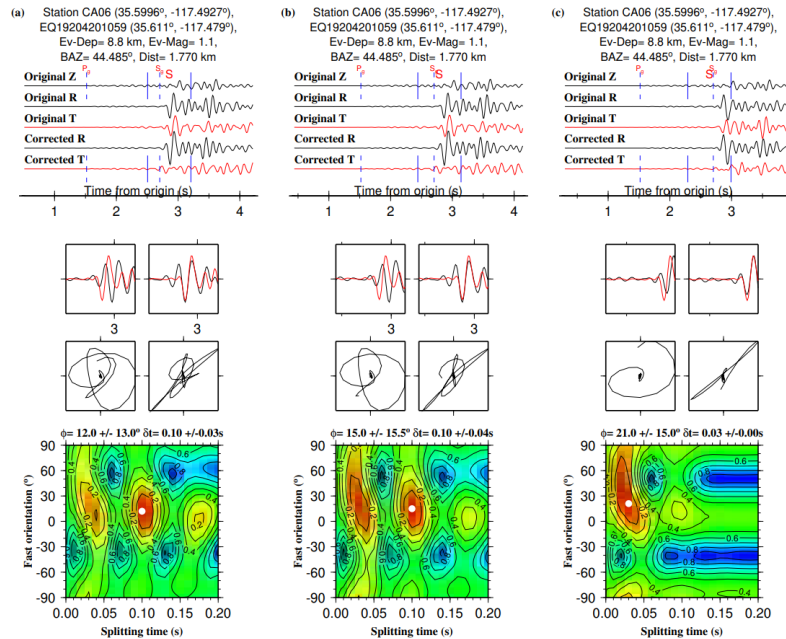


Figure A6. Another event recorded by Station CA06 to demonstrate the effects of cycle skipping. In this case results shown in (c) are the optimal results.

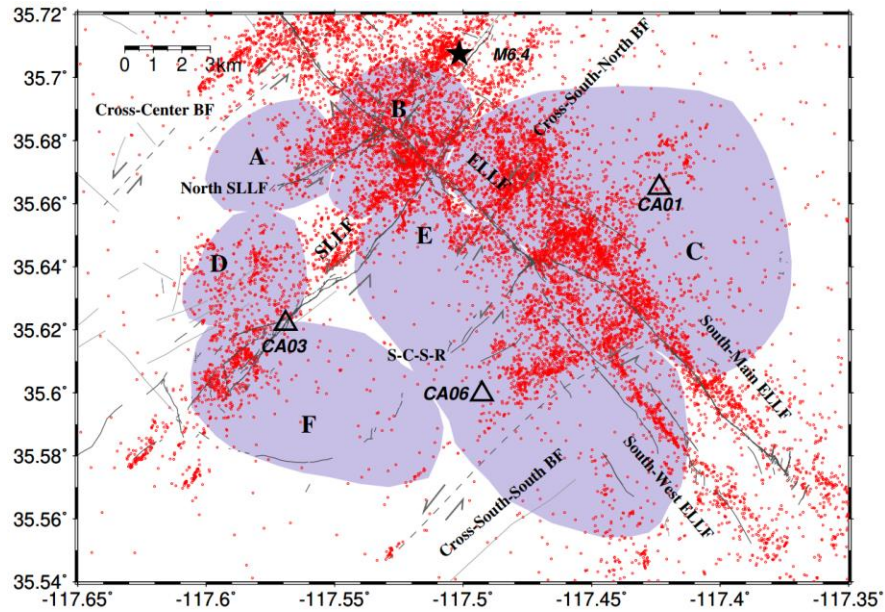


Figure A7. Distribution of earthquakes (red dots) in the study area occurred from 1 January 2019 to 31 December 2019.

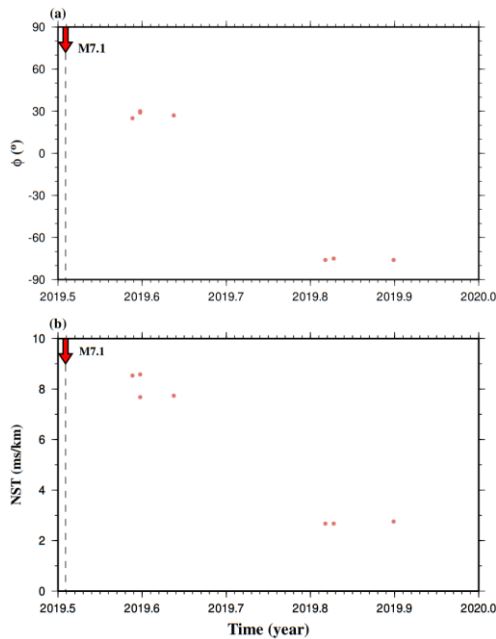


Figure A8. Temporal variations of the resulting shear wave splitting parameters described in Section 4.5.

REFERENCES

- Alford, R. M. (1986). Shear data in presence of azimuthal anisotropy: 56th Annals International Meeting. *Society Exploration Geophysics, Expanded Abstract*, 476–479. <https://doi.org/10.1190/1.1893036>
- Ando, M., Ishikawa, Y., & Wada, H. (1980). S-wave anisotropy in the upper mantle under a volcanic area in Japan. *Nature*, 286(5768), 43–46. <https://doi.org/10.1038/286043a0>
- Aster, R. C., Shearer, P. M., & Berger, J. (1990). Quantitative measurements of shear wave polarizations at the Anza Seismic Network, southern California: Implications for shear wave splitting and earthquake prediction. *Journal of Geophysical Research*, 95(B8), 12449–12473. <https://doi.org/10.1029/JB095iB08p12449>
- Audet, P. (2015). Layered crustal anisotropy around the San Andreas fault near Parkfield, California. *Journal of Geophysical Research: Solid Earth*, 120(5), 3527–3543. <https://doi.org/10.1002/2014JB011821>
- Barnhart, W. D., Hayes, G. P., & Gold, R. D. (2019). The July 2019 Ridgecrest, California, Earthquake Sequence: Kinematics of slip and stressing in Cross-fault Ruptures. *Geophysical Research Letters*, 46(21), 11859–11867. <https://doi.org/10.1029/2019GL084741>
- Bastow, I. D., Pilidou, S., Kendall, J. M., & Stuart, G. W. (2010). Melt-induced seismic anisotropy and magma assisted rifting in Ethiopia: Evidence from surface waves. *Geochemistry, Geophysics, Geosystems*, 11(6). <https://doi.org/10.1029/2010GC003036>
- Bokelmann, G. H. R., & Harjes, H. P. (2000). Evidence for temporal variation of seismic velocity within the upper continental crust. *Journal of Geophysical Research*, 105, 23879–23894. <https://doi.org/10.1029/2000JB900207>
- Boness, N. L., & Zoback, M. D. (2004). Stress-induced seismic velocity anisotropy and physical properties in the SAFOD Pilot Hole in Parkfield, California. *Geophysical Research Letters*, 31, L15S17. <https://doi.org/10.1029/2003GL019020>
- Boness, N. L., & Zoback, M. D. (2006). Mapping stress and structurally controlled crustal shear velocity anisotropy in California. *Geology*, 34(10), 825–828. <https://doi.org/10.1130/G22309.1>

- Booth, D. C., & Crampin, S. (1985). Shear-wave polarizations on a curved wavefront at an isotropic free surface. *Geophysical Journal International*, 83(1), 31–45. <https://doi.org/10.1111/j.1365-246X.1985.tb05154.x>
- Brocher, T. M., & Christensen, N. I. (1990). Seismic anisotropy due to preferred mineral orientation observed in shallow crustal rocks in southern Alaska. *Geology*, 18(8), 737–740. [https://doi.org/10.1130/0091-7613\(1990\)018<0737:SADTPM>2.3.CO;2](https://doi.org/10.1130/0091-7613(1990)018<0737:SADTPM>2.3.CO;2)
- Chen, K., Avouac, J. P., Aati, S., Milliner, C., Zheng, F., & Shi, C. (2020). Cascading and pulse-like ruptures during the 2019 Ridgecrest earthquakes in the Eastern California Shear Zone. *Nature communications*, 11(1), 1–8. <https://doi.org/10.1038/s41467-019-13750-w>
- Cochran, E. S., Vidale, J. E., & Li, Y.-G. (2003). Near-fault anisotropy following the Hector Mine earthquake. *Journal of Geophysical Research: Solid Earth*, 108(B9). <https://doi.org/10.1029/2002JB002352>
- Cochran, E. S., Wolin, E., McNamara, D. E., Yong, A., Wilson, D., Alvarez, M., et al. (2020). The U.S. Geological Survey's rapid seismic array deployment for the 2019 Ridgecrest earthquake sequence. *Seismological Research Letters*, 91(4), 1952–1960. <https://doi.org/10.1785/0220190296>
- Crampin, S. (1978). Seismic-wave propagation through a cracked solid: Polarization as a possible dilatancy diagnostic. *Geophysical Journal International*, 53(3), 467–496. <https://doi.org/10.1111/j.1365-246X.1978.tb03754.x>
- Crampin, S. (1987). Geological and industrial implications of extensive-dilatancy anisotropy. *Nature*, 328(6130), 491–496. <https://doi.org/10.1038/328491a0>
- Crampin, S. (1991). Wave propagation through fluid-filled inclusions of various shapes: Interpretation of extensive-dilatancy anisotropy. *Geophysical Journal International*, 107, 611–623. <https://doi.org/10.1111/j.1365-246X.1991.tb05705.x>
- Crampin, S. (1993). Arguments for EDA. *Canadian Journal of Exploration Geophysics*, 29(1), 18-30.
- Crampin, S. (1994). The fracture criticality of crustal rocks. *Geophysical Journal International*, 118(2), 428–438. <https://doi.org/10.1111/j.1365-246X.1994.tb03974.x>
- Crampin, S., Booth, D. C., Evans, R., Peacock, S., & Fletcher, J. B. (1990). Changes in shear wave splitting at Anza near the time of the North Palm Springs Earthquake. *Journal of Geophysical Research*, 95(B7), 11197. <https://doi.org/10.1029/jb095ib07p11197>

- Duan, H., Chu, Z., Zhang, S., Yang, C., Chen, J., & Lei, J. (2022). Analysis of coseismic slip distributions and stress variations of the 2019 Mw 6.4 and 7.1 earthquakes in Ridgecrest, California. *Tectonophysics*, 831, 229343. <https://doi.org/10.1016/j.tecto.2022.229343>
- DuRoss, C. B. et al. (2020). Surface displacement distributions for the July 2019 Ridgecrest, California, Earthquake Ruptures. *Bulletin of the Seismological Society of America*, 110(4), 1400–1418. <https://doi.org/10.1785/0120200058>
- Fielding, E. J., Liu, Z., Stephenson, O. L., Zhong, M., Liang, C., Moore, A., et al. (2020). Surface deformation related to the 2019Mw 7.1 and 6.4 Ridgecrest Earthquakes in California from GPS, SAR Interferometry, and SAR Pixel Offsets. *Seismological Research Letters*, 91(4), 2035–2046. <https://doi.org/10.1785/0220190302>
- Gao, S., Davis, P. M., Liu, H., Slack, P. D., Rigor, A. W., Zorin, Y. A., et al. (1997). SKS splitting beneath continental rift zones. *Journal of Geophysical Research: Solid Earth*, 102(B10), 22781–22797. <https://doi.org/10.1029/97JB01858>
- Gao, Y., & Crampin, S. (2003). Temporal variations of shear-wave splitting in field and laboratory studies in China. *Journal of Applied Geophysics*, 54(3-4), 279–287. <https://doi.org/10.1016/j.jappgeo.2003.01.002>
- Gao, Y., & Crampin, S. (2004). Observations of stress relaxation before earthquakes. *Geophysical Journal International*, 157(2), 578–582. <https://doi.org/10.1111/j.1365-246x.2004.02207.x>
- Gao, Y., Wang, P., Zheng, S., Wang, M., Chen, Y., & Zhou, H. (1998). Temporal changes in shear-wave splitting at an isolated swarm of small earthquakes in 1992 near Dongfang, Hainan Island, southern China. *Geophysical Journal International*, 135(1), 102–112. <https://doi.org/10.1046/j.1365-246x.1998.00606.x>
- Gerst, A. (2003). Temporal changes in seismic anisotropy as a new eruption forecasting tool?, (M.Sc. thesis). (<http://hdl.handle.net/10063/13>). 184 pp., Victoria University of Wellington, Wellington, New Zealand.
- Hauksson, E., Yoon, C., Yu, E., Andrews, J. R., Alvarez, M., Bhadha, R., & Thomas, V. (2020). Caltech/USGS Southern California Seismic Network (SCSN) and Southern California Earthquake Data Center (SCEDC): Data availability for the 2019 Ridgecrest sequence. *Seismological Research Letters*, 91(4), 1961–1970. <https://doi.org/10.1785/0220190290>
- Hardebeck, J. L. (2020). A stress-similarity triggering model for aftershocks of the Mw 6.4 and 7.1 Ridgecrest earthquakes. *Bulletin of the Seismological Society of America*, 110(4), 1716–1727. <https://doi.org/10.1785/0120200015>

- Hiramatsu, Y., Honma, H., Saiga, A., Furumoto, M., & Ooida, T. (2005). Seismological evidence on characteristic time of crack healing in the shallow crust. *Geophysical Research Letters*, *32*(9). <https://doi.org/10.1029/2005GL022657>
- Hiramatsu, Y., Iwatsuki, K., Ueyama, S., & Iidaka, T. (2010). Spatial variation in shear wave splitting of the upper crust in the zone of inland high strain rate, central Japan. *Earth Planets and Space*, *62*(9), 675–684. <https://doi.org/10.5047/eps.2010.08.003>
- Holtzman, B. K., Groebner, N. J., Zimmerman, M. E., Ginsberg, S. B., & Kohlstedt, D. L. (2003). Stress-driven melt segregation in partially molten rocks. *Geochemistry, Geophysics, Geosystems*, *4*(5). <https://doi.org/10.1029/2001GC000258>
- Jiang, E., Liu, K. H., Gao, Y., Fu, X., & Gao, S. S. (2021). Spatial Variations of Upper Crustal Anisotropy along the San Jacinto Fault Zone in Southern California: Constraints from Shear Wave Splitting Analysis. *Journal of Geophysical Research: Solid Earth*, *126*(4), e2020JB020876. <https://doi.org/10.1029/2020JB020876>
- Johnson, J. H., Prejean, S., Savage, M. K., & Townend, J. (2010). Anisotropy, repeating earthquakes, and seismicity associated with the 2008 eruption of Okmok volcano, Alaska. *Journal of Geophysical Research: Solid Earth*, *115*(B9). <https://doi.org/10.1029/2009JB006991>
- Kaneshima, S. (1990). Origin of crustal anisotropy: Shear wave splitting studies in Japan. *Journal of Geophysical Research: Solid Earth*, *95*(B7), 11121–11133. <https://doi.org/10.1029/JB095iB07p11121>
- Keir, D., Kendall, J. M., Ebinger, C. J., & Stuart, G. W. (2005). Variations in late syn-rift melt alignment inferred from shear-wave splitting in crustal earthquakes beneath the Ethiopian rift. *Geophysical Research Letters*, *32*(23). <https://doi.org/10.1029/2005GL024150>
- Leary, P. C., Crampin, S., & McEvilly, T. V. (1990). Seismic fracture anisotropy in the Earth's crust: An overview. *Journal of Geophysical Research: Solid Earth*, *95*(B7), 11105–11114. <https://doi.org/10.1029/jb095ib07p11105>
- Li, T., Gu, Y. J., Wang, Z., Wang, R., Chen, Y., Song, T. R. A., & Wang, R. (2019). Spatiotemporal variations in crustal seismic anisotropy surrounding induced earthquakes near Fox Creek, Alberta. *Geophysical Research Letters*, *46*, 5180–5189. <https://doi.org/10.1029/2018GL081766>
- Li, Z., & Peng, Z. (2017). Stress-and structure-induced anisotropy in southern California from two decades of shear wave splitting measurements. *Geophysical Research Letters*, *44*(19), 9607–9614. <https://doi.org/10.1002/2017GL075163>

- Li, Z., Zhang, H., & Peng, Z. (2014). Structure-controlled seismic anisotropy along the Karadere–Düzce branch of the North Anatolian Fault revealed by shear-wave splitting tomography. *Earth and Planetary Science Letters*, *391*, 319–326. <https://doi.org/10.1016/j.epsl.2014.01.046>
- Liu, C., Lay, T., Brodsky, E. E., Dascher-Cousineau, K., & Xiong, X. (2019). Coseismic rupture process of the large 2019 Ridgecrest earthquakes from joint inversion of geodetic and seismological observations. *Geophysical Research Letters*, *46*(21), 11820–11829. <https://doi.org/10.1029/2019GL08494>
- Liu, K. H., Gao, S. S., Gao, Y., & Wu, J. (2008). Shear wave splitting and mantle flow associated with the deflected Pacific slab beneath northeast Asia. *Journal of Geophysical Research: Solid Earth*, *113*(B1). <https://doi.org/10.1029/2007JB005178>
- Liu, K. H., & Gao, S. S. (2013). Making reliable shear-wave splitting measurements. *Bulletin of the Seismological Society of America*, *103*(5), 2680–2693. <https://doi.org/10.1785/0120120355>
- Liu, Y., Crampin, S., & Main, I. (1997). Shear-wave anisotropy: spatial and temporal variations in time delays at Parkfield, Central California. *Geophysical Journal International*, *130*(3), 771–785. <https://doi.org/10.1111/j.1365-246X.1997.tb01872.x>
- Liu, Y., Teng, T. L., & Ben-Zion, Y. (2004). Systematic analysis of shear-wave splitting in the aftershock zone of the 1999 Chi-Chi, Taiwan, earthquake: shallow crustal anisotropy and lack of precursory variations. *Bulletin of the Seismological Society of America*, *94*(6), 2330–2347. <https://doi.org/10.1785/0120030139>
- Liu, Y., Zhang, H., Thurber, C., & Roecker, S. (2008). Shear wave anisotropy in the crust around the San Andreas fault near Parkfield: Spatial and temporal analysis. *Geophysical Journal International*, *172*(3), 957–970. <https://doi.org/10.1111/j.1365-246X.2007.03618.x>
- Liu, Y., Zhang, H., Kendall, J. M., & Wookey, J. (2021). Conjugate fault deformation revealed by aftershocks of the 2013 Mw6.6 Lushan earthquake and seismic anisotropy tomography. *Geophysical Research Letters*, *48*, e2021GL092563. <https://doi.org/10.1029/2021GL092563>
- Lucente, F. P., De Gori, P., Margheriti, L., Piccinini, D., Di Bona, M., Chiarabba, C., & Agostinetti, N. P. (2010). Temporal variation of seismic velocity and anisotropy before the 2009 MW 6.3 L'Aquila earthquake, Italy. *Geology*, *38*(11), 1015–1018. <https://doi.org/10.1130/G31463.1>

- Matcham, I., Savage, M. K., & Gledhill, K. R. (2000). Distribution of seismic anisotropy in the subduction zone beneath the Wellington region, New Zealand. *Geophysical Journal International*, *140*(1), 1–10. <https://doi.org/10.1046/j.1365-246x.2000.00928.x>
- Miller, V., & Savage, M. (2001). Changes in seismic anisotropy after volcanic eruptions: Evidence from Mount Ruapehu. *Science*, *293*(5538), 2231–2233. <https://doi.org/10.1126/science.1063463>
- Nuttli, O. (1961). The effect of the Earth's surface on the S wave particle motion. *Bulletin of the Seismological Society of America*, *51*(2), 237–246. <https://doi.org/10.1785/BSSA0510020237>
- Okaya, D., Christensen, N. I., Ross, Z. E., & Wu, F. T. (2016). Terrane-controlled crustal shear wave splitting in Taiwan. *Geophysical Research Letters*, *43*(2), 556–563. <https://doi.org/10.1002/2015GL066446>
- Peng, Z., & Ben-Zion, Y. (2004). Systematic analysis of crustal anisotropy along the Karadere-Düzce branch of the North Anatolian fault. *Geophysical Journal International*, *159*, 253–274. <https://doi.org/10.1111/j.1365-246X.2004.02379.x>
- Plesch, A., Shaw, J. H., Ross, Z. E., & Hauksson, E. (2020). Detailed 3D fault representations for the 2019 Ridgecrest, California, earthquake sequence. *Bulletin of the Seismological Society of America*, *110*(4), 1818–1831. <https://doi.org/10.1785/0120200053>
- Ponti, D.J., Blair, J.L., Rosa, C.M., Thomas, K., Pickering, A.J., Akciz, S., et al. (2020). Documentation of Surface Fault Rupture and Ground-Deformation Features Produced by the 4 and 5 July 2019 M w 6.4 and M w 7.1 Ridgecrest Earthquake Sequence. *Seismological Society of America*, *91*(5), 2942–2959. <https://doi.org/10.1785/0220190322>
- Ross, Z. E. et al. (2019). Hierarchical interlocked orthogonal faulting in the 2019 Ridgecrest earthquake sequence. *Science*, *366*(6463), 346–351. <https://doi.org/10.1126/science.aaz0109>
- Savage, M. K., Ferrazzini, V., Peltier, A., Rivemale, E., Mayor, J., Schmid, A., et al. (2015). Seismic anisotropy and its precursory change before eruptions at Piton de la Fournaise volcano, La Réunion. *Journal of Geophysical Research: Solid Earth*, *120*(5), 3430–3458. <https://doi.org/10.1002/2014JB011665>
- Savage, M. K., Wessel, A., Teanby, N. A., & Hurst, A. W. (2010). Automatic measurement of shear wave splitting and applications to time varying anisotropy at Mount Ruapehu volcano, New Zealand. *Journal of Geophysical Research: Solid Earth*, *115*(B12). <https://doi.org/10.1029/2010JB007722>

- Sayers, C. M. (1994). The elastic anisotropy of shales. *Journal of Geophysical Research: Solid Earth*, 99(B1), 767–774. <https://doi.org/10.1029/93JB02579>
- Shelly, D. R. (2020). A high-resolution seismic catalog for the initial 2019 Ridgecrest earthquake sequence: Foreshocks, aftershocks, and faulting complexity. *Seismological Research Letters*, 91(4), 1971–1978. <https://doi.org/10.1785/0220190309>
- Sheng, S., & Meng, L. (2020). Stress field variation during the 2019 Ridgecrest earthquake sequence. *Geophysical Research Letters*, 47(15), e2020GL087722. <https://doi.org/10.1029/2020gl087722>
- Shi, Y. T., Gao, Y., Shen, X. Z., & Liu, K. H. (2020). Multiscale spatial distribution of crustal seismic anisotropy beneath the northeastern margin of the Tibetan plateau and tectonic implications of the Haiyuan fault. *Tectonophysics*, 774, 228274. <https://doi.org/10.1016/j.tecto.2019.228274>
- Silver, P. G., & Chan, W. W. (1991). Shear wave splitting and subcontinental mantle deformation. *Journal of Geophysical Research*, 96(B10), 16429–16454. <https://doi.org/10.1029/91JB00899>
- Tadokoro, K., & Ando, M. (2002). Evidence for rapid fault healing derived from temporal changes in S wave splitting. *Geophysical Research Letters*, 29(4), 6–10. <https://doi.org/10.1029/2001GL013644>
- Volti, T., & Crampin, S. (2003). A four-year study of shear-wave splitting in Iceland: 2. Temporal changes before earthquakes and volcanic eruptions. *Geological Society, London, Special Publications*, 212(1), 135–149. <https://doi.org/10.1144/GSL.SP.2003.212.01.09>
- Walsh, E. (2012). Measuring shear wave splitting using the Silver and Chan method, (MS thesis). (<http://hdl.handle.net/10063/2608>). 157 pp., Victoria University of Wellington, Wellington.
- Wang, X., & Zhan, Z. (2020). Seismotectonics and fault geometries of the 2019 Ridgecrest sequence: Insight from aftershock moment tensor catalog using 3-D Green's functions. *Journal of Geophysical Research: Solid Earth*, 125(5), e2020JB019577. <https://doi.org/10.1029/2020jb019577>
- White, M. C., Fang, H., Catchings, R. D., Goldman, M. R., Steidl, J. H., & Ben-Zion, Y. (2021). Detailed traveltimes tomography and seismic catalogue around the 2019 Mw 7.1 Ridgecrest, California, earthquake using dense rapid-response seismic data. *Geophysical Journal International*, 227(1), 204–227. <https://doi.org/10.1093/gji/ggab224>

- Wills, C. J. (1988). Little Lake and Airport Lake fault zones. *California, California Division of Mines and Geology Fault Evaluation Report FER-199*.
- Wu, C., Tian, X., Xu, T., Liang, X., Chen, Y., Zhu, G., et al. (2019). Upper-crustal anisotropy of the conjugate strike-slip fault zone in Central Tibet analyzed using local earthquakes and shear-wave splitting. *Bulletin of the Seismological Society of America*, 109(5), 1968–1984. <https://doi.org/10.1785/0120180333>
- Zhang, Z., & Schwartz, S. Y. (1994). Seismic anisotropy in the shallow crust of the Loma Prieta segment of the San Andreas fault system. *Journal of Geophysical Research: Solid Earth*, 99(B5), 9651–9661. <https://doi.org/10.1029/94JB00241>
- Zinke, J. C., & Zoback, M. D. (2000). Structure-related and stress-induced shear-wave velocity anisotropy: Observations from microearthquakes near the Calaveras Fault in Central California. *Bulletin of the Seismological Society of America*, 90(5), 1305–1312. <https://doi.org/10.1785/01199>

SECTION

2. CONCLUSIONS

In this study, we systematically examined the local-scale spatially varying anisotropic structures in the Earth's upper crust and upper mantle, as well as the associated formation mechanisms of laterally heterogeneous anisotropy, utilizing the shear wave splitting method.

Our research is composed of two sub-projects. In the first project, we investigated the piercing-point-dependent azimuthal anisotropy using the teleseismic data collected on the northeastern edge of the Sichuan Basin in central China. A total of 360 pairs of resulting XKS splitting parameters indicate that:

- (1) The consideration of laterally heterogeneous anisotropy structures is essential for the interpretation of splitting measurements.
- (2) The resulting SWS measurements display systematic azimuthal variations in ϕ with no 90° or 180° periodicity, which indicates the piercing point-dependent anisotropy.
- (3) Spatial coherency analysis results suggest that the anisotropy source mostly locates in the depth of ~ 250 km, which is comparable to the depth of the bottom of lithosphere.
- (4) The observations can be explained by APM-related simple shear in the transitional layer between the lithosphere and the asthenosphere, and mantle flow deflected by the thick lithospheric root in the upper asthenosphere.

The second project is focused on the local-scale laterally heterogeneous anisotropy of the upper crust in the 2019 M7.1 Ridgecrest earthquake aftershock zone. Some significant conclusions are revealed based on the analyses of 803 pairs of observed direct shear wave splitting parameters and are listed below:

- (1) The pronounced spatial and temporal variations imply that the mixed mechanisms of the regional stress field and shear action of growth faults may be responsible for the heterogeneous anisotropy in the seismogenic zone beneath the 2019 Ridgecrest aftershock zone.
- (2) Seismic anisotropy far from the fault zone or with a less developed fault zone, such as the area to the northeast of the ELLF and around the North SLLF, is mainly controlled by regional compressive stress.
- (3) The structure-induced anisotropy dominates the shear zones of the active faults in the area to the southwest of the ELLF and exhibits consistency between the direction of fault strikes and fast orientations.
- (4) The asymmetry of rock strength across the ELLF and significant variations in the width of the damaged zone along the ELLF are implied by the different formation mechanisms of the uppermost crustal anisotropy.
- (5) A clear temporal variation of both the orientation and strength of anisotropy near the intersection between the ELLF and the Cross-South-North blind fault may indicate the rapid healing of the NE-SW striking ELLF.

BIBLIOGRAPHY

- Ando, M., Ishikawa, Y., & Wada, H. (1980). S-wave anisotropy in the upper mantle under a volcanic area in Japan. *Nature*, **286**, 43–46.
- Ando, M., Ishikawa, Y., & Yamazaki, F. (1983). Shear wave polarization anisotropy in the upper mantle beneath Honshu, Japan. *Journal of Geophysical Research: Solid Earth*, **88**(B7), 5850–5864. <https://doi.org/10.1029/jb088ib07p05850>.
- Barnhart, W. D., Hayes, G. P., & Gold, R. D. (2019). The July 2019 Ridgecrest, California, Earthquake Sequence: Kinematics of slip and stressing in Cross-fault Ruptures. *Geophysical Research Letters*, *46*(21), 11859–11867. <https://doi.org/10.1029/2019GL084741>.
- Ben Ismail, W., & Mainprice, D. (1998). An olivine fabric database: An overview of upper mantle fabrics and seismic anisotropy. *Tectonophysics*, **296**, 145-157. [https://doi.org/10.1016/S0040-1951\(98\)00141-3](https://doi.org/10.1016/S0040-1951(98)00141-3).
- Boness, N. L., & Zoback, M. D. (2004). Stress-induced seismic velocity anisotropy and physical properties in the SAFOD Pilot Hole in Parkfield, California. *Geophysical Research Letters*, *31*, L15S17. <https://doi.org/10.1029/2003GL019020>.
- Boness, N. L., & Zoback, M. D. (2006). Mapping stress and structurally controlled crustal shear velocity anisotropy in California. *Geology*, *34*(10), 825-828. <https://doi.org/10.1130/G22309.1>.
- Crampin, S. (1978). Seismic-wave propagation through a cracked solid: Polarization as a possible dilatancy diagnostic. *Geophysical Journal International*, *53*(3), 467–496. <https://doi.org/10.1111/j.1365-246X.1978.tb03754.x>.
- Crampin, S. (1987). Geological and industrial implications of extensive-dilatancy anisotropy. *Nature*, *328*(6130), 491-496. <https://doi.org/10.1038/328491a0>.
- Crampin, S. (1991). Wave propagation through fluid-filled inclusions of various shapes: Interpretation of extensive-dilatancy anisotropy. *Geophysical Journal International*, *107*, 611–623. <https://doi.org/10.1111/j.1365-246X.1991.tb05705.x>
- Crampin, S. (1993). Arguments for EDA. *Canadian Journal of Exploration Geophysics*, *29*(1), 18-30.
- Crampin, S. (1994). The fracture criticality of crustal rocks. *Geophysical Journal International*, *118*(2), 428–438. <https://doi.org/10.1111/j.1365-246X.1994.tb03974.x>.

- Cochran, E. S., Vidale, J. E., & Li, Y.-G. (2003). Near-fault anisotropy following the Hector Mine earthquake. *Journal of Geophysical Research: Solid Earth*, *108*(B9). <https://doi.org/10.1029/2002JB002352>.
- DuRoss, C. B. et al. (2020). Surface displacement distributions for the July 2019 Ridgecrest, California, Earthquake Ruptures. *Bulletin of the Seismological Society of America*, *110*(4), 1400–1418. <https://doi.org/10.1785/0120200058>.
- Fouch, M. J. & Rondenay, S. (2006). Seismic anisotropy beneath stable continental interiors, *Physics of the Earth and Planetary Interiors*. **158**(2-4), 292–320. <https://doi.org/10.1016/j.pepi.2006.03.024>.
- Fuchs, K. (1977). Seismic anisotropy of the subcrustal lithosphere as evidence for dynamical processes in the upper mantle. *Geophysical Journal International*, **49**(1), 167–179. <https://doi.org/10.1111/j.1365-246x.1977.tb03707.x>.
- Gao, S., Davis, P. M., Liu, H., Slack, P. D., Zorin, Y. A., Mordvinova, V. V., Kozhevnikov, V.M. & Meyer, R.P. (1994). Seismic anisotropy and mantle flow beneath the Baikal rift zone. *Nature*, **371**(6493), 149. <https://doi.org/10.1038/371149a0>.
- Gao, S. S. & Liu, K. H. (2012). AnisDep: A FORTRAN program for the estimation of the depth of anisotropy using spatial coherency of shear-wave splitting parameters. *Computers & Geosciences*, **49**, 330–333. <https://doi.org/10.1016/j.cageo.2012.01.020>.
- Hess, H. H. (1964). Seismic Anisotropy of the Uppermost Mantle under Oceans. *Nature*, **203**(4945), 629–631. <https://doi.org/10.1038/203629a0>.
- Leary, P. C., Crampin, S., & McEvilly, T. V. (1990). Seismic fracture anisotropy in the Earth's crust: An overview. *Journal of Geophysical Research: Solid Earth*, *95*(B7), 11105–11114. <https://doi.org/10.1029/jb095ib07p11105>.
- Li, Z., & Peng, Z. (2017). Stress-and structure-induced anisotropy in southern California from two decades of shear wave splitting measurements. *Geophysical Research Letters*, *44*(19), 9607–9614. <https://doi.org/10.1002/2017GL075163>.
- Liu, C., Lay, T., Brodsky, E. E., Dascher-Cousineau, K., & Xiong, X. (2019). Coseismic rupture process of the large 2019 Ridgecrest earthquakes from joint inversion of geodetic and seismological observations. *Geophysical Research Letters*, *46*(21), 11820–11829. <https://doi.org/10.1029/2019GL084949>.

- Liu, K. H. & Gao, S. S. (2011). Estimation of the Depth of Anisotropy Using Spatial Coherency of Shear-Wave Splitting Parameters. *Bulletin of the Seismological Society of America*, **101**(5), 2153–2161. <https://doi.org/10.1785/0120100258>.
- Liu, K. H. & Gao, S. S. (2013). Making Reliable Shear-Wave Splitting Measurements. *Bulletin of the Seismological Society of America*, **103**(5), 2680–2693. <https://doi.org/10.1785/0120120355>.
- Liu, Y., Crampin, S., & Main, I. (1997). Shear-wave anisotropy: spatial and temporal variations in time delays at Parkfield, Central California. *Geophysical Journal International*, **130**(3), 771–785. <https://doi.org/10.1111/j.1365-246X.1997.tb01872.x>.
- Long, M. D. & Silver, P. G. (2009). Shear wave splitting anisotropy: Measurements, interpretation, and new directions. *Surveys In Geophysics*, **30**, 407–461. <https://doi.org/10.1007/s10712-009-9075-1>.
- Mainprice, D. & Nicolas, A. (1989). Development of shape and lattice preferred orientations: Application to the seismic anisotropy of the lower crust. *Journal of Structural Geology*, **11**(1-2), 175–189. [https://doi.org/10.1016/0191-8141\(89\)90042-4](https://doi.org/10.1016/0191-8141(89)90042-4).
- Miller, V., & Savage, M. (2001). Changes in seismic anisotropy after volcanic eruptions: Evidence from Mount Ruapehu. *Science*, **293**(5538), 2231–2233. <https://doi.org/10.1126/science.1063463>.
- Ohuchi, T. & Irifune, T. (2013). Development of A-type olivine fabric in water-rich deep upper mantle. *Earth and Planetary Science Letters*, **362**, 20–30. <https://doi.org/10.1016/j.epsl.2012.11.029>.
- Peng, Z., & Ben-Zion, Y. (2004). Systematic analysis of crustal anisotropy along the Karadere-Düzce branch of the North Anatolian fault. *Geophysical Journal International*, **159**, 253–274. <https://doi.org/10.1111/j.1365-246X.2004.02379.x>.
- Ponti, D.J., Blair, J.L., Rosa, C.M., Thomas, K., Pickering, A.J., Akciz, S., Angster, S., Avouac, J.P., Bachhuber, J., Bacon, S., et al. (2020). Documentation of Surface Fault Rupture and Ground-Deformation Features Produced by the 4 and 5 July 2019 M w 6.4 and M w 7.1 Ridgecrest Earthquake Sequence. *Seismological Society of America*, **91**(5), 2942–2959. <https://doi.org/10.1785/0220190322>.
- Ross, Z. E. et al. (2019). Hierarchical interlocked orthogonal faulting in the 2019 Ridgecrest earthquake sequence. *Science*, **366**(6463), 346–351. <https://doi.org/10.1126/science.aaz0109>.

- Shelly, D. R. (2020). A high-resolution seismic catalog for the initial 2019 Ridgecrest earthquake sequence: Foreshocks, aftershocks, and faulting complexity. *Seismological Research Letters*, *91*(4), 1971-1978. <https://doi.org/10.1785/0220190309>.
- Savage, M. K. (1999). Seismic anisotropy and mantle deformation: What have we learned from shear wave splitting? *Rev. Geophys.*, *37*(1), 65–106. <https://doi.org/10.1029/98rg02075>.
- Silver, P. G. (1996). Seismic anisotropy beneath the continents: Probing the depths of geology. *Annu. Rev. Earth Planet. Sci.*, *24*(1), 385–432. <https://doi.org/10.1146/annurev.earth.24.1.385>.
- Silver, P. G., & Chan, W. W. (1991). Shear wave splitting and subcontinental mantle deformation. *Journal of Geophysical Research*, *96*(B10), 16429-16454. <https://doi.org/10.1029/91JB00899>.
- Silver, P. G. & Savage, M. K. (1994). The Interpretation of Shear-Wave Splitting Parameters In the Presence of Two Anisotropic Layers. *Geophysical Journal International*, *119*(3), 949–963. <https://doi.org/10.1111/j.1365-246x.1994.tb04027.x>.
- Vinnik, L. P., Makeyeva, L. I., Milev, A. & Usenko, A. Y. (1992). Global patterns of azimuthal anisotropy and deformations in the continental mantle. *Geophysical Journal International*, *111*(3), 433–447. <https://doi.org/10.1111/j.1365-246x.1992.tb02102.x>.
- Zhang, S. & Karato, S.-I. (1995). Lattice preferred orientation of olivine aggregates deformed in simple shear. *Nature*, *375*(6534), 774–777. <https://doi.org/10.1038/375774a0>.
- Zhang, Z., & Schwartz, S. Y. (1994). Seismic anisotropy in the shallow crust of the Loma Prieta segment of the San Andreas fault system. *Journal of Geophysical Research: Solid Earth*, *99*(B5), 9651-9661. <https://doi.org/10.1029/94JB00241>.
- Zinke, J. C., & Zoback, M. D. (2000). Structure-related and stress-induced shear-wave velocity anisotropy: Observations from microearthquakes near the Calaveras Fault in Central California. *Bulletin of the Seismological Society of America*, *90*(5), 1305-1312. <https://doi.org/10.1785/011199>.

VITA

Yan Jia received her bachelor's degree in Resource Exploration Engineering from Northeast Petroleum University in June 2018. She received another bachelor's degree in Geology and Geophysics from the Missouri University of Science and Technology in July 2018. She joined Dr. Kelly H. Liu and Dr. Stephen S. Gao's geophysics research group in the Geology and Geophysics program at Missouri University of Science and Technology in August 2018.

From 2019 to 2022, Yan worked as a teaching assistant or research assistant in the Geology and Geophysics program at Missouri University of Science and Technology. She was an active member of the American Geophysical Union (AGU) and the Society of Exploration Geophysics (SEG). She presented her research works at the AGU annual meeting in 2019, 2020, and 2021, which are focused on the Earth's crust and mantle structures and geodynamic models using the shear wave splitting and receiver function methods. She was offered the honorable mention of the Jeffery Spooner Outstanding Graduate Scholar Award and Publication Award in 2021.

In December 2022, she received her Ph.D. degree in Geology and Geophysics from the Missouri University of Science and Technology.